Characterization of halogen-bridged binuclear metal complexes as hybridized two-band materials

Shoji Yamamoto
Department of Physics, Okayama University, Tsushima, Okayama 700-8530, Japan
(Received 27 July 2000; published 13 March 2001)

We study the electronic structure of halogen-bridged binuclear metal (MMX) complexes with a two-band Peierls-Hubbard model. Based on a symmetry argument, various density-wave states are derived and characterized. The ground-state phase diagram is drawn within the Hartree-Fock approximation, while the thermal behavior is investigated using a quantum Monte Carlo method. All the calculations conclude that a typical MMX compound $Pt_2(CH_3CS_2)_4I$ should indeed be regarded as a d-p-hybridized two-band material, where the oxidation of the halogen ions must be observed even in the ground state, whereas another MMX family $(NH_4)_4[Pt_2(P_2O_5H_2)_4X]$ may be treated as single-band materials.

DOI: 10.1103/PhysRevB.63.125124 PACS number(s): 71.10.Hf, 71.45.Lr, 75.30.Fv, 75.40.Mg

I. INTRODUCTION

The family of transition-metal (M) linear-chain complexes containing bridging halogens (X) has a long history of research[1–3] especially in the chemical field. The conventional class[4] of these materials, which we refer to as MX chains, is represented by the Wolffram red salts ($M=Pt, X=Cl$) and has been fascinating both chemists and physicists due to its novel properties, such as intense and dichroic charge-transfer absorption, strong resonance enhancement of Raman spectra, and luminescence with large Stokes shift, which all originate in the mixed-valence ground state. On the other hand, the synthesis of NiX compounds[5,6] that exhibit monovalence magnetic ground states aroused renewed interest in this system. Substituting the metals, bridging halogens, ligand molecules, and counteranions surrounding the one-dimensional chains, the tunability of the ground-state electronic structure was fully revealed.[7] A pressure-induced reverse Peierls instability[8] was also demonstrated. All these observations can be understood as the competition between the Peierls and Mott insulators.[9] Intrinsic multiband effects, together with competing electron-electron and electron-phonon interactions, raise a possibility of further ground states appearing, such as incommensurate (long-period) charge-density waves,[10] spin-Peierls states,[11] and density waves on the halogen sublattice.[12] A leading group[13] in Los Alamos National Laboratory presented an extensive two-band-model study covering the ground-state properties, excitation spectra, and quantum lattice fluctuations. The research trend is now shifting toward mixed-metal complexes,[14,15] where the ground-state degeneracy is lifted and therefore the relaxation process of photogenerated excitons via solitons or polarons can efficiently be controlled.

In an attempt to explore further this unique system, a new class of these materials, which we refer to as MMX chains, has been synthesized, where binuclear metal units are bridged by halogen ions. Thus-far synthesized MMX-chain compounds are classified into two groups: $M_2(dta)_4I$ [$M=Pt, Ni$; dta=dithioacetate=$CH_3CS_2^-$ (Refs. 16 and 17)] and $R_4[Pt_2(pop)_4X]\cdot nH_2O$ ($X=Cl, Br, I$; $R=K, NH_4$, etc.; pop=diphosphonate=$H_2P_2O_5^{2-}$),[18] which we hereafter refer to as dta and pop complexes. The binucleation of the metal sites does much more than simply increase the internal degrees of freedom of the electronic configuration:

(i) The formal oxidation state of metal ions is $2.5+$, that is, a mixed valency of M^{2+} and M^{3+}, in MMX chains, whereas it is $3+$, that is, a mixed valency of M^{2+} and M^{4+}, in MX chains. There exists an unpaired electron per one metal-dimer unit of trapped valence M^{2+}-M^{3+}, while none at all in the corresponding unit of trapped valence M^{2+}-M^{4+}.

(ii) The direct M-M overlap contributes to the reduction of the effective on-site Coulomb repulsion and thus electrons can be more itinerant in MMX chains.

(iii) In the MX-chain system, metals are tightly locked together due to the hydrogen bonds between the amino groups of the ligands and the counteranions. Therefore any dimerization of the metal sublattice has not yet been observed. In the MMX-chain system, adjacent metals are locked to each other by the surrounding ligands, but the metal-dimer moiety itself is rather movable especially in the dta complexes with neutral chain structures. Although there still exist weak van der Waals contacts between ligands against the Peierls instability in the dta complexes, $Pt_2(dta)_4I$ has recently been reported to exhibit a dimerization of the metal sublattice.[19]

(iv) Owing to the neutral chain structure, the band filling of the dta complexes might be varied.

Thus, the new class of the halogen-bridged metal complexes is highly potential in every aspect. Further efforts to synthesize general polynuclear metal complexes[20] stimulate our interest all the more.

The physical properties of the MMX-chain system are not so well established as the accumulated chemical knowledge. There is a hot argument about the valence structures of MMX chains. So far four types of the oxidation states have been pointed out, which are illustrated in Fig. 1. All but type (a) are accompanied by lattice distortion, where the X sites are displaced, maintaining the translational symmetry in (b), the M_2 sublattice is dimerized in (c), and the X sublattice is dimerized in (d). In this notation, type (a) represents spin-density-wave states of any kind as well as the paramagnetic (metallic) state.

The ground-state valence structure of the Cl- and Br-bridged Pt complexes of the pop family was extensively investigated by resonance Raman spectroscopy,[21] x-ray single-crystal structure analyses,[22,23] solid-state ^{31}P nuclear-magnetic-resonance measurements,[24] and polarized optical

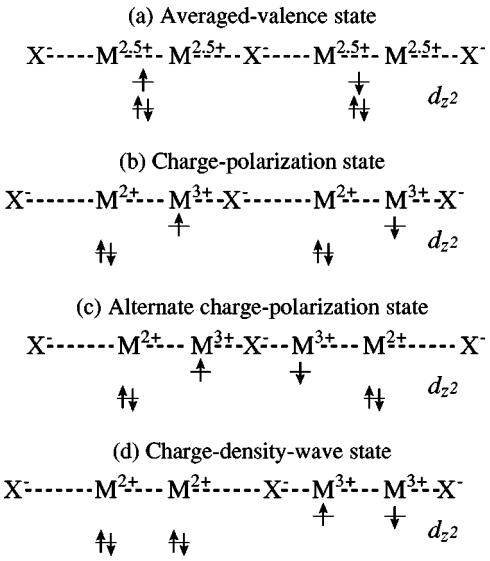

FIG. 1. Schematic representation of electronic structures of the MMX chain, where the electrons in the M d_{z^2} orbitals are regarded as efficient, while the X p_z orbitals, which are fully occupied in the crystal rearrangement, are treated as irrelevant to the low-energy physics.

spectra[25] and was concluded to be type (d). However, due to the small Peierls gap, the ground states of these materials can be tuned with pressure from the strongly *valence-trapped* state (d) toward the *valence-delocalized* state (a) [or possibly (c) (Ref. 26)], where the pressure mainly contributes to the increase of the electron transfer between neighboring Pt_2 moieties. Such charge fluctuations become more remarkable when bridging halogens are replaced by I.[27] The valence transition is sensitive to the radius of the countercations and the number of the water molecules as well.

For the dta complexes, on the other hand, the electronic structures seem to be more complicated and less established. X-ray photoelectron spectra of the Ni complexes[17] suggest the valence delocalization on the regular chain structure (a), which is convincing on the analogy of NiX chains with magnetic ground states characterized as Mott-Hubbard insulators.[28] Although early measurements[16,17] on the Pt complexes of the dta series implied their structural similarities with the Ni complexes and the valence delocalization at room temperature, recent experiments[29] have reported another scenario for the valence structure of the Pt complexes: With decreasing temperature, there occurs a metal-semiconductor transition, that is, a transition from the averaged-valence state (a) to the trapped-valence state (b) at 300 K, and further transition to the charge-ordering mode (c) follows around 80 K. The valence structure (c) accompanied by the metal-sublattice dimerization is all the more interesting in relation to spin-Peierls fluctuations, which have never yet been observed in the MX-chain system.

In response to such stimulative observations, we here calculate the electronic structure of MMX compounds employing a $\frac{5}{6}$-filled two-band model. In the notation of Fig. 1, the filled X p_z orbitals are rendered irrelevant. It is sometimes assumed in phenomenological arguments and experimental investigations that unless the system is photoexcited and/or activated by hole doping, the halogen ions contribute no effective electron to the low-energy physics. The goal of this paper is to give a criterion for when the $\frac{3}{4}$-filled single-band approximation is valid or invalid. We calculate ground-state phase diagrams within the Hartree-Fock approximation, where we analytically classify and characterize possible density-wave solutions making full use of symmetry properties. Based on the thus-revealed ground-state properties, we further carry out quantum Monte Carlo calculations of the thermal properties. Extensive analytical and numerical calculations bring us a wide view of the d-p-hybridized two-band electron-phonon system.

II. HARTREE-FOCK CALCULATION BASED ON A SYMMETRY ARGUMENT

A. Model Hamiltonian and its symmetry properties

We introduce the $\frac{5}{6}$-filled one-dimensional two-band three-orbital extended Peierls-Hubbard Hamiltonian:

$$\mathcal{H}=\frac{K}{2}\sum_{n}(l_{1:n}^2+l_{2:n}^2)+\sum_{n,s}[(\varepsilon_M-\beta l_{1:n})n_{1:n,s}+(\varepsilon_M+\beta l_{2:n})n_{2:n,s}+\varepsilon_X n_{3:n,s}]-\sum_{n,s}[(t_{MX}-\alpha l_{1:n})a_{1:n,s}^{\dagger}a_{3:n,s}$$
$$+(t_{MX}+\alpha l_{2:n})a_{2:n,s}^{\dagger}a_{3:n,s}+t_{MM}a_{1:n,s}^{\dagger}a_{2:n-1,s}+\mathrm{H.c.}]+\sum_{n}(U_M n_{1:n,+}n_{1:n,-}+U_M n_{2:n,+}n_{2:n,-}+U_X n_{3:n,+}n_{3:n,-})$$
$$+\sum_{n,s,s'}(V_{MX}n_{1:n,s}n_{3:n,s'}+V_{MX}n_{2:n,s}n_{3:n,s'}+V_{MM}n_{1:n,s}n_{2:n-1,s'}), \tag{2.1}$$

where $n_{i:n,s}=a_{i:n,s}^{\dagger}a_{i:n,s}$ with $a_{i:n,s}^{\dagger}$ being the creation operator of an electron with spin $s=\pm$ (up and down) for the M d_{z^2} ($i=1,2$) or X p_z ($i=3$) orbital in the nth MXM unit, and $l_{i:n}=u_{3:n}-u_{i:n}$ with $u_{i:n}$ being the chain-direction displacement of the metal ($i=1,2$) or halogen ($i=3$) in the nth MXM unit from its equilibrium position. α and β are, respectively, the intersite and intrasite electron-phonon (e-ph) coupling constants, while K is the metal-halogen spring constant. We assume, based on the thus-far reported experimental observations, that every M_2 moiety is not deformed,

TABLE I. Symmetry operations of the group elements $g \in \mathbf{G}$ on the electron operators.

	l	C_2	$u(\boldsymbol{e},\theta)$	t
$a^\dagger_{1:k,s}$	$e^{-ik}a^\dagger_{1:k,s}$	$a^\dagger_{2:-k,s}$	$\Sigma_{s'}[u(\boldsymbol{e},\theta)]_{ss'}a^\dagger_{1:k,s'}$	$(-1)^s a^\dagger_{1:-k,-s}$
$a^\dagger_{2:k,s}$	$e^{-ik}a^\dagger_{2:k,s}$	$a^\dagger_{1:-k,s}$	$\Sigma_{s'}[u(\boldsymbol{e},\theta)]_{ss'}a^\dagger_{2:k,s'}$	$(-1)^s a^\dagger_{2:-k,-s}$
$a^\dagger_{3:k,s}$	$e^{-ik}a^\dagger_{3:k,s}$	$a^\dagger_{3:-k,s}$	$\Sigma_{s'}[u(\boldsymbol{e},\theta)]_{ss'}a^\dagger_{3:k,s'}$	$(-1)^s a^\dagger_{3:-k,-s}$
$a^\dagger_{1:k+\pi,s}$	$-e^{-ik}a^\dagger_{1:k+\pi,s}$	$e^{-(2\pi/3)i}a^\dagger_{2:-k+\pi,s}$	$\Sigma_{s'}[u(\boldsymbol{e},\theta)]_{ss'}a^\dagger_{1:k+\pi,s'}$	$(-1)^s e^{-(2\pi/3)i}a^\dagger_{1:-k+\pi,-s}$
$a^\dagger_{2:k+\pi,s}$	$-e^{-ik}a^\dagger_{2:k+\pi,s}$	$e^{(2\pi/3)i}a^\dagger_{1:-k+\pi,s}$	$\Sigma_{s'}[u(\boldsymbol{e},\theta)]_{ss'}a^\dagger_{2:k+\pi,s'}$	$(-1)^s e^{(2\pi/3)i}a^\dagger_{2:-k+\pi,-s}$
$a^\dagger_{3:k+\pi,s}$	$-e^{-ik}a^\dagger_{3:k+\pi,s}$	$a^\dagger_{3:-k+\pi,s}$	$\Sigma_{s'}[u(\boldsymbol{e},\theta)]_{ss'}a^\dagger_{3:k+\pi,s'}$	$(-1)^s a^\dagger_{3:-k+\pi,-s}$

namely, $u_{1:n}=u_{2:n-1}$. ε_M and ε_X are the on-site energies (electron affinities) of isolated metal and halogen atoms, respectively. Since ε_M is usually larger than ε_X, we neglect the weak alternation of the halogen-ion on-site energies. The electron hoppings between these levels are modeled by t_{MM} and t_{MX}, whereas the electron-electron Coulomb interactions by U_M, U_X, V_{MM}, and V_{MX}. Coulomb interactions between neighboring metal and halogen ions may in principle alternate in accordance with lattice displacements in a two-band description. However, such a Coulomb-phonon coupling is usually neglected renormalizing β under the mean-field treatment of $\Sigma_s n_{3:n,s}$. We take N for the number of unit cells in the following. Let us rewrite the Hamiltonian compactly in the momentum space as

$$\begin{aligned}\mathcal{H}=&\sum_{i,j}\sum_{k,q}\sum_{s,s'}\langle i{:}k+q,s|t|j{:}k,s'\rangle a^\dagger_{i:k+q,s}a_{j:k,s'}\\&+\frac{1}{2}\sum_{i,j,m,n}\sum_{k,k',q}\sum_{s,s',t,t'}a^\dagger_{i:k+q,s}a^\dagger_{m:k',t}a_{n:k'+q,t'}a_{j:k,s'}\\&\times\langle i{:}k+q,s;m{:}k',t|v|j{:}k,s';n{:}k'+q,t'\rangle\\&+\frac{K}{2}\sum_q[u_{1:q}u^*_{1:q}+u_{2:q}u^*_{2:q}+2u_{3:q}u^*_{3:q}\\&-(e^{iq/3}u_{1:q}u^*_{3:q}+e^{-iq/3}u_{2:q}u^*_{3:q}+\text{c.c.})],\end{aligned}\tag{2.2}$$

where we have set the unit-cell length (the distance between neighboring halogen ions) equal to unity. The momentum representation of the interactions can straightforwardly be obtained from the Fourier transform of the original Hamiltonian (2.1) and we learn

$$\langle i{:}k+q,s|t|j{:}k,s'\rangle=\langle i{:}k+q|t|j{:}k\rangle\delta_{ss'},\tag{2.3}$$

$$\begin{aligned}&\langle i{:}k+q,s;m{:}k',t|v|j{:}k,s';n{:}k'+q,t'\rangle\\&\quad=\langle i{:}k+q;m{:}k'|v|j{:}k;n{:}k'+q\rangle\delta_{ss'}\delta_{tt'}.\end{aligned}\tag{2.4}$$

The most essential process of the Hartree-Fock approximation must be the introduction of order parameters. A symmetry argument[30,31] allows us to systematically derive density-wave solutions and reduce the following numerical efforts to the minimum necessary. As far as we consider the normal states, that is, unless the gauge symmetry is broken, the symmetry group of the present system is given by

$$\mathbf{G}=\mathbf{P}\times\mathbf{S}\times\mathbf{T},\tag{2.5}$$

where $\mathbf{P}=\mathbf{L}\wedge\mathbf{C}_2$ is the space group of a linear chain with the one-dimensional translation group $\mathbf{L}$ whose basis vector is the unit-cell translation l, $\mathbf{S}$ is the group of spin rotation, and $\mathbf{T}$ is the group of time reversal. Group actions on the electron operators are defined in Table I, where $l\in\mathbf{L}$, $C_2\in\mathbf{C}_2$, $u(\boldsymbol{e},\theta)=\sigma^0\cos(\theta/2)-(\boldsymbol{\sigma}\cdot\boldsymbol{e})\sin(\theta/2)\in\mathbf{S}$, and $t\in\mathbf{T}$ with σ^0 and $\boldsymbol{\sigma}=(\sigma^x,\sigma^y,\sigma^z)$ being the 2×2 unit matrix and a vector composed of the Pauli matrices, respectively.

Let $\check{G}$ denote the irreducible representations of $\mathbf{G}$ over the real number field, where their representation space is spanned by the Hermitian operators $\{a^\dagger_{i:k,s}a_{j:k',s'}\}$. There is a one-to-one correspondence between $\check{G}$ and broken-symmetry phases of density-wave type.[32,33] Any representation $\check{G}$ is obtained as a Kronecker product of the irreducible real representations of $\mathbf{P}$, $\mathbf{S}$, and $\mathbf{T}$:

$$\check{G}=\check{P}\otimes\check{S}\otimes\check{T}.\tag{2.6}$$

$\check{P}$ is characterized by an ordering vector q in the Brillouin zone and an irreducible representation of its little group $\mathbf{P}(q)$, and is therefore labeled $q\check{P}(q)$. The relevant representations of $\mathbf{S}$ are given by

$$\begin{aligned}&\check{S}^0(u(\boldsymbol{e},\theta))=1\quad(\text{nonmagnetic}),\\&\check{S}^1(u(\boldsymbol{e},\theta))=O(u(\boldsymbol{e},\theta))\quad(\text{magnetic}),\end{aligned}\tag{2.7}$$

where $O(u(\boldsymbol{e},\theta))$ is the 3×3 orthogonal matrix satisfying $u(\boldsymbol{e},\theta)\boldsymbol{\sigma}^\lambda u^\dagger(\boldsymbol{e},\theta)=\Sigma_{\mu=x,y,z}[O(u(\boldsymbol{e},\theta))]_{\lambda\mu}\boldsymbol{\sigma}^\mu$ $(\lambda=x,y,z)$, whereas those of $\mathbf{T}$ by

$$\begin{aligned}&\check{T}^0(t)=1\quad(\text{symmetric}),\\&\check{T}^1(t)=-1\quad(\text{antisymmetric}).\end{aligned}\tag{2.8}$$

The representations $\check{P}\otimes\check{S}^0\otimes\check{T}^0$, $\check{P}\otimes\check{S}^1\otimes\check{T}^1$, $\check{P}\otimes\check{S}^0\otimes\check{T}^1$, and $\check{P}\otimes\check{S}^1\otimes\check{T}^0$ correspond to charge-density-wave (CDW), spin-density-wave (SDW), charge-current-wave (CCW), and spin-current-wave (SCW) states, respectively. Here in one dimension, the current-wave states either result in the one-way uniform flow or break the charge-conservation law and are therefore less interesting. We consider density waves of

$q=0$ and $q=\pi$, which are labeled Γ and X, respectively. Since $\mathbf{P}(\Gamma)=\mathbf{P}(X)=\mathbf{C}_2$, $\check{P}(\Gamma)$ and $\check{P}(X)$ are either the A (C_2-symmetric) or B (C_2-antisymmetric) representation of $\mathbf{C}_2$.

B. Broken-symmetry solutions

Now the mean-field Hamiltonian is given by

$$\mathcal{H}_{\mathrm{HF}}=\sum_{i,j}\sum_{k,s,s'}\sum_{\lambda}[x_{ij}^{\lambda}(\Gamma;k)a_{i:k,s}^{\dagger}a_{j:k,s'} + x_{ij}^{\lambda}(X;k)a_{i:k+\pi,s}^{\dagger}a_{j:k,s'}]\sigma_{ss'}^{\lambda}. \tag{2.9}$$

Here the self-consistent fields $x_{ij}^{\lambda}(\Gamma;k)$ and $x_{ij}^{\lambda}(X;k)$ are described as

$$x_{ij}^{0}(\Gamma;k)=\langle i:k|t|j:k\rangle+\sum_{m,n}\sum_{k'}\rho_{nm}^{0}(\Gamma;k') \times(2\langle i:k;m:k'|v|j:k;n:k'\rangle - \langle i:k;m:k'|v|n:k';j:k\rangle), \tag{2.10}$$

$$x_{ij}^{0}(X;k)=\langle i:k+\pi|t|j:k\rangle+\sum_{m,n}\sum_{k'}\rho_{nm}^{0}(X;k'+\pi) \times(2\langle i:k+\pi;m:k'|v|j:k;n:k'+\pi\rangle - \langle i:k+\pi;m:k'|v|n:k'+\pi;j:k\rangle), \tag{2.11}$$

$$x_{ij}^{z}(\Gamma;k)=-\sum_{m,n}\sum_{k'}\rho_{nm}^{z}(\Gamma;k') \times\langle i:k;m:k'|v|n:k';j:k\rangle, \tag{2.12}$$

$$x_{ij}^{z}(X;k)=-\sum_{m,n}\sum_{k'}\rho_{nm}^{z}(X;k'+\pi) \times\langle i:k+\pi;m:k'|v|n:k'+\pi;j:k\rangle, \tag{2.13}$$

in terms of the density matrices

$$\rho_{ij}^{\lambda}(\Gamma;k)=\frac{1}{2}\sum_{s,s'}\langle a_{j:k,s}^{\dagger}a_{i:k,s'}\rangle_{\mathrm{HF}}\sigma_{ss'}^{\lambda}, \tag{2.14}$$

$$\rho_{ij}^{\lambda}(X;k)=\frac{1}{2}\sum_{s,s'}\langle a_{j:k+\pi,s}^{\dagger}a_{i:k,s'}\rangle_{\mathrm{HF}}\sigma_{ss'}^{\lambda}, \tag{2.15}$$

where $\langle\cdots\rangle_{\mathrm{HF}}$ denotes the quantum average in a Hartree-Fock eigenstate. We note that no helical SDW solution ($\lambda=x,y$) is obtained from the present Hamiltonian. We decompose the Hamiltonian (2.9) as

$$\mathcal{H}_{\mathrm{HF}}=\sum_{D=A,B}\sum_{K=\Gamma,X}\sum_{\lambda=0,z}h_{KD}^{\lambda}. \tag{2.16}$$

Here the irreducible component h_{KD}^{λ} can be obtained through a general formula

$$h_{KD}^{\lambda}=\frac{d^{(D)}}{g}\sum_{p\in\mathbf{C}_2}\chi^{(D)}(p)p\cdot x_{ij}^{\lambda}(K;k)a_{i:k,s}^{\dagger}a_{j:k,s'}\sigma_{ss'}^{\lambda}, \tag{2.17}$$

where $\chi^{(D)}(p)$ is the irreducible character of the D representation for the group element p, $g(=2)$ is the order of $\mathbf{C}_2$, and $d^{(D)}$ $(=1)$ is the dimension of D. Thus we obtain the broken-symmetry Hamiltonian for the representation $KD\otimes\check{S}^{i}\otimes\check{T}^{i}$ as $\mathcal{H}_{\mathrm{HF}}(K;D)=h_{\Gamma A}^{0}+h_{KD}^{\lambda}$, where $\lambda=0$ $(i=0)$ or $\lambda=z$ $(i=1)$. We explicitly show h_{KD}^{λ} in Appendix A.

In order to characterize each phase, we define local order parameters. The charge and spin densities on site i at the nth MXM unit are, respectively, given by

$$d_{i:n}=\sum_{s}\langle a_{i:n,s}^{\dagger}a_{i:n,s}\rangle_{\mathrm{HF}}, \tag{2.18}$$

$$s_{i:n}^{z}=\frac{1}{2}\sum_{s,s'}\langle a_{i:n,s}^{\dagger}a_{i:n,s'}\rangle_{\mathrm{HF}}\sigma_{ss'}^{z}, \tag{2.19}$$

while the bond and spin bond orders between site i at the nth MXM unit and site j at the mth MXM unit are, respectively, defined as

$$p_{i:n;j:m}=\sum_{s}\langle a_{i:n,s}^{\dagger}a_{j:m,s}\rangle_{\mathrm{HF}}, \tag{2.20}$$

$$t_{i:n;j:m}^{z}=\frac{1}{2}\sum_{s,s'}\langle a_{i:n,s}^{\dagger}a_{j:n,s'}\rangle_{\mathrm{HF}}\sigma_{ss'}^{z}. \tag{2.21}$$

Though $p_{i:n;j:m}$ and $t_{i:n;j:m}^{z}$ can generally be complex, their imaginary parts are necessarily zero in our argument. The order parameters can also be described in terms of the density matrices (2.14) and (2.15). Demanding that the density matrices should have the same symmetry properties as their *host Hamiltonian,* we can qualitatively characterize all the density-wave solutions. We briefly describe their properties in the following and explicitly show the analytic consequences of the symmetry argument in Appendix B.

(a) $\Gamma A\otimes\check{S}^{0}\otimes\check{T}^{0}$: The paramagnetic state with the full symmetry **G**, abbreviated as PM.

(b) $\Gamma B\otimes\check{S}^{0}\otimes\check{T}^{0}$: Bond order wave with polarized charge densities on the M_2 moieties, abbreviated as BOW.

(c) $XA\otimes\check{S}^{0}\otimes\check{T}^{0}$: Charge-density wave on the X sublattice with alternate polarized charge densities on the M_2 moieties, abbreviated as X-CDW.

(d) $XB\otimes\check{S}^{0}\otimes\check{T}^{0}$: Charge density wave on the M sublattice, abbreviated as M-CDW.

(e) $\Gamma A\otimes\check{S}^{1}\otimes\check{T}^{1}$: Ferromagnetism on both M_2 and X sublattices, abbreviated as FM.

(f) $\Gamma B\otimes\check{S}^{1}\otimes\check{T}^{1}$: Spin bond order wave with polarized spin densities on the M_2 moieties, abbreviated as SBOW.

(g) $XA\otimes\check{S}^{1}\otimes\check{T}^{1}$: Spin-density wave on the X sublattice with alternate polarized spin densities on the M_2 moieties, abbreviated as X-SDW.

(h) $XB\otimes\check{S}^{1}\otimes\check{T}^{1}$: Spin-density wave on the M sublattice, abbreviated as M-SDW.

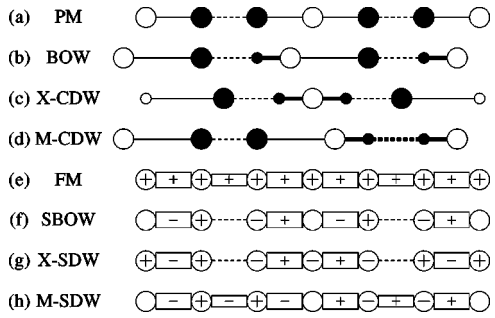

FIG. 2. Schematic representation of possible density-wave states, where the various circles and segments qualitatively represent the variation of local electron densities and bond orders, respectively, whereas the signs ± in circles and strips describe the alternation of local spin densities and spin bond orders, respectively. Circles shifted from the regular position qualitatively represent lattice distortion, which is peculiar to nonmagnetic phases.

Here, $\overline{\rho}^{\lambda}_{ij}(K;k)$ and $\tilde{\rho}^{\lambda}_{ij}(K;k)$ denote the real and imaginary parts of $\rho^{\lambda}_{ij}(K;k)$, respectively. All the phases are schematically shown in Fig. 2. The nonmagnetic broken-symmetry phases (a)–(d), respectively, correspond to the oxidation states (a)–(d) in Fig. 1 in this order.

So far little interest has been taken in the electronic state of the halogen ions in the full belief that in comparison with the $M\ d_{z^2}$ orbitals, the $X\ p_z$ orbitals are stably filled and less effective, at least, in the ground state. Such an idea may relatively be valid for MX chains, but it is not the case any more for MMX chains where the metal sublattice can be distorted. Our symmetry argument suggests that the X-CDW (alternate charge-polarization) state should be characterized by the charge-density wave on the X sublattice rather than any modulation on the M_2 sublattice. If we add up the charge and spin densities on the adjacent metal sites in every M_2 moiety, they indeed modulate in M-CDW and M-SDW, whereas they are uniform in X-CDW and X-SDW. Alternate charge densities on the X sublattice necessarily mean the oxidation of the halogen ions.

We learn much more from the symmetry argument. Magnetic instabilities are generally not coupled with phonons. Specifying vanishing and nonvanishing density matrices and obtaining the *symmetry-definite* Hartree-Fock energy expression, we find which type of electronic correlation is effective in stabilizing each density-wave state. The halogen on-site Coulomb repulsion U_X stabilizes X-SDW and destabilizes X-CDW, respectively, while it is much less relevant to the M-type density-wave states. Though the intradimer different-site Coulomb repulsion V_{MM} has little effect on the X-type density-wave states, it efficiently stabilizes both M-CDW and M-SDW states. This is somewhat surprising because the repulsive interaction V_{MM} favors charge disproportionation in the M_2 moiety at the naivest consideration. The V_{MM} stabilization of the M-type density-wave states comes from the Hamiltonian component related to the field b^{λ}_{XB} [see Eqs. (A4), (A8), and (A12)]. We find that V_{MM} favorably contributes to the modulation of the intradimer electron transfer. The following numerical calculations show that the situation $V_{MM}>V_{MX}$ generally stabilizes the M-type density-wave states, whereas those of the X type are relatively stabilized under $V_{MM}<V_{MX}$, provided any other factor, such as the alternation of transfer integrals, is rendered irrelevant.

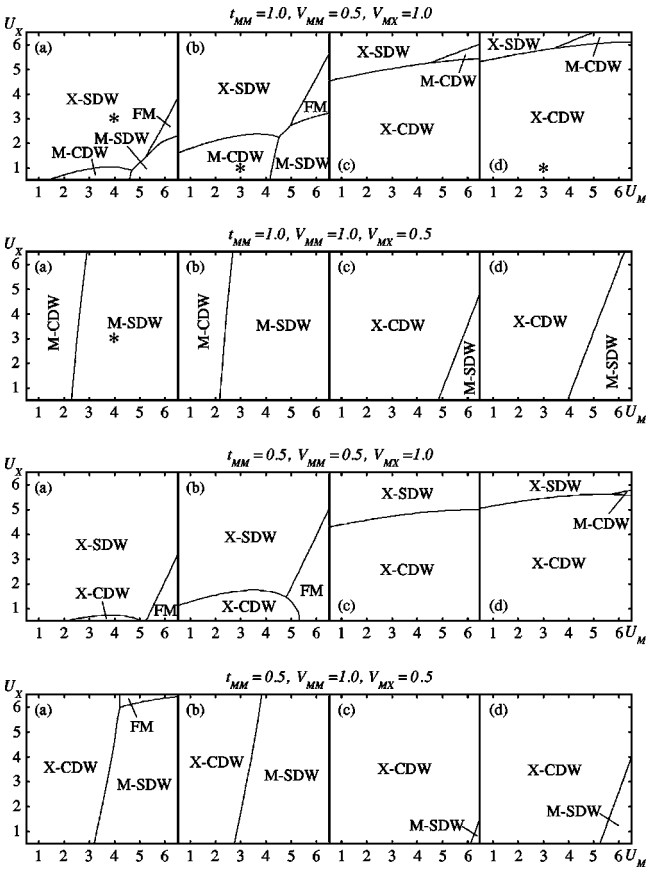

FIG. 3. Typical ground-state phase diagrams at $\frac{5}{6}$ band filling: (a) $\varepsilon_M-\varepsilon_X\equiv\Delta\varepsilon=0.2$, $\alpha=0.6$, $\beta=1.8$; (b) $\Delta\varepsilon=1.0$, $\alpha=0.6$, $\beta=1.8$; (c) $\Delta\varepsilon=0.2$, $\alpha=1.8$, $\beta=0.6$; (d) $\Delta\varepsilon=1.0$, $\alpha=1.8$, $\beta=0.6$. The rest of the parameters are common to each set of four figures and are indicated beside them. Asterisks in the phase diagrams are for the convenience of later arguments.

C. Ground-state phase diagrams

Let us observe competing ground states numerically. We calculate the Hartree-Fock energies $\langle\mathcal{H}\rangle_{\mathrm{HF}}$ at a sufficiently low temperature ($k_{\mathrm{B}}T/t_{MX}=0.025$) in the thermodynamic limit ($N\rightarrow\infty$). We show in Fig. 3 typical ground-state phase diagrams at $\frac{5}{6}$ band filling, where the strength of any interaction is indicated setting both t_{MX} and K equal to unity. Despite the large amount of parameters, the phase diagrams bring us a general view of the ground-state properties:

(i) Fundamentally, on-site Coulomb repulsions are advantageous to SDW states, whereas intersite repulsions are advantageous to CDW states. This can be easily understood by an analogy of the *U-V competition* between CDW and SDW states in the single-band extended Hubbard model. With increasing U, the antiferromagnetic spin alignments are replaced by FM spin alignments.

(ii) The site-diagonal electron-phonon coupling β is favorable for M-CDW, while the intersite coupling α is

favourable for *X*-CDW. This is also convincing when we simplify the argument employing a single-band model. Without the *X* p_z orbitals, the dimerization of the *X* sublattice is simply modeled by modulating *on-site* electron affinities, while that of the M_2 sublattice results in the modulation of *intersite* hopping integrals just as polyacetylene.[34] Thus, it is likely in the pop complexes that the interchain locking of the M_2 sublattices due to counterions is effectively realized with the parametrization $\beta > \alpha$. α-versus-β phase diagrams have recently been calculated within a single-band approximation by Kuwabar and Yonemitsu,[35] where the competition from this point of view can be observed in more detail. They report that β and α favor *M*-CDW and *X*-CDW, respectively, but *X*-CDW is much more widely stabilized to the ground state than *M*-CDW, which is consistent with the present observations.

(iii) With respect to Coulomb interactions, U_M and V_{MM} contribute to the *M*-type density waves, while U_X and V_{MX} to those of the *X*-type. If we neglect the intersite Coulomb repulsions and any modulation of transfer integrals, the phase diagram is rather understandable: For small *U*, *M*-CDW ($\alpha < \beta$) or *X*-CDW ($\alpha \gtrsim \beta$); for large *U*, FM; otherwise, *M*-SDW ($U_{\mathrm{M}} \gtrsim U_{\mathrm{X}} - \Delta\varepsilon$) or *X*-SDW ($U_M \lesssim U_X - \Delta\varepsilon$). $\Delta\varepsilon \equiv \varepsilon_M - \varepsilon_X$ may be recognized as the orbital-energy correction to the *M-X competition*.[36]

(iv) The competition between *M*-CDW and *X*-CDW is sensitive to the modulation of transfer integrals as well. Provided α is not so large as β, *M*-CDW is stabilized under $t_{MM} > t_{MX}$, whereas it is replaced by *X*-CDW under $t_{MM} \lesssim t_{MX}$. The orbital hybridization within every M_2 moiety is essential in the *valence-trapped M*-CDW state, while it is the overlap of the d_{σ^*} orbitals on neighboring M_2 moieties that stabilizes the *valence-delocalized X*-CDW state. Based on semiempirical quantum-chemical band calculations, Borshch *et al.*[37] pointed out a possibility of the *X*-CDW-type valence structure being stabilized in this context. They revealed, restricting their argument to the $Pt_2(dta)_4I$ compound, that twisting of the dta ligand reduces the electronic communication by π delocalization between adjacent metal sites and ends in charge disproportionation within the M_2 moiety. On the other hand, employing a single-band model, Baeriswyl and Bishop[38] pioneeringly suggested that with increasing *M-X-M* interdimer transfer integral, the distortion of the halogen sublattice should shrink and in the end the metal sublattice may begin to dimerize. Though their argument was mainly devoted to the *MX*-chain system, it is valid enough for the *MMX*-chain system as well. Such a behavior was indeed observed[8] applying pressure to a *MMX* material $K_4[Pt_2(pop)_4Br]\cdot 3H_2O$, which may be understood as a pressure-induced reverse Peierls instability.

At $\frac{5}{6}$ band filling, due to the perfect nesting of the Fermi surface with respect to $q = \pi$ phonons, $X(q = \pi)$ phases are predominantly stabilized. Therefore, doping of the system generally contributes to the stabilization of $\Gamma(q = 0)$ phases, though any doping of *MMX* chains has not yet been reported. At $\frac{4}{6}$ band filling, for example, an interesting competition between BOW and SBOW (Ref. 39) is observed, that is, the competition between *site-centered* CDW and SDW states is replaced by that between *bond-centered* CDW and SDW states.

Now we are convinced that a single-band description of the *M*-type density waves (*M*-CDW and *M*-SDW) may be well justified, whereas the halogen p_z orbitals should explicitly be taken into consideration in describing those of the *X*-type (*X*-CDW and *X*-SDW). In the next section, we further support this criterion using a quantum Monte Carlo technique. The pop and dta families will fully be characterized as approximate d_{z^2}-single-band materials and real *d-p*-hybridized two-band materials, respectively.

III. QUANTUM MONTE CARLO APPROACH

A. Numerical procedure

We employ a quantum Monte Carlo method[40] based on the checkerboard-type decomposition[41] of the partition function. We simulate the Hamiltonian (2.1), namely, we here make an adiabatic description of the phonon field.[42] Starting with an arbitrary electron and lattice configuration, we update the electron configuration under the frozen phonon field and then update the lattice configuration under the fixed electron configuration by the heat-bath algorithm. At each Monte Carlo step, under the constraint $u_{1:n} = u_{2:n-1}$, every site moves right or left by a sufficiently small unit Δ_{unit} or otherwise stays at the present position: $\tilde{u}_{i:n} \to \tilde{u}_{i:n} + \delta\tilde{u}_{i:n}$; $\delta\tilde{u}_{i:n} = \Delta_{\mathrm{unit}}, -\Delta_{\mathrm{unit}}, 0$, where $\tilde{u}_{i:n} = \alpha u_{i:n}/t_{MX}$. Δ_{unit} is set equal to 0.02. According to such movements of lattice sites, the bond configuration is updated as

$$l_{1:n} \to l_{1:n} - \delta u_{1:n}, \quad l_{2:n-1} \to l_{2:n-1} - \delta u_{1:n}$$

$$\text{for } u_{1:n} \to u_{1:n} + \delta u_{1:n},$$

$$l_{1:n} \to l_{1:n} + \delta u_{3:n}, \quad l_{2:n} \to l_{2:n} + \delta u_{3:n}$$

$$\text{for } u_{3:n} \to u_{3:n} + \delta u_{3:n},$$

where the total length of the lattice is kept unchanged.

Since it is difficult to handle negative weights with the world-line Monte Carlo algorithm,[40] we further modify the original model (2.1) taking the metal-halogen hopping matrix elements to be

$$\langle 1{:}n|t|3{:}n\rangle = \begin{cases} t_{\mathrm{MX}} - \alpha l_{1:n} & \text{for } \tilde{u}_{3:n} - \tilde{u}_{1:n} < 1 \\ 0 & \text{for } \tilde{u}_{3:n} - \tilde{u}_{1:n} \geq 1, \end{cases} \tag{3.1}$$

$$\langle 2{:}n|t|3{:}n\rangle = \begin{cases} t_{\mathrm{MX}} + \alpha l_{2:n} & \text{for } \tilde{u}_{2:n} - \tilde{u}_{3:n} < 1 \\ 0 & \text{for } \tilde{u}_{2:n} - \tilde{u}_{3:n} \geq 1. \end{cases} \tag{3.2}$$

As the atoms move away from each other, the overlap matrix elements go to zero and do not change sign. Therefore, the above modification makes sense from a physical point of view and may be justified with not-so-large coupling constants.

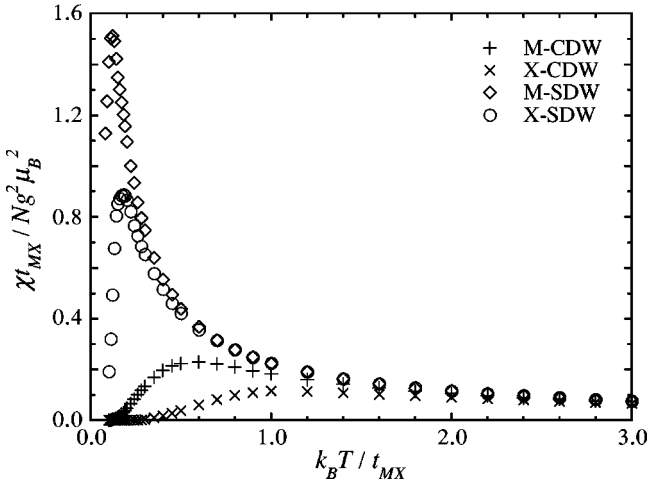

FIG. 4. Temperature dependences of the magnetic susceptibility at typical parametrizations: $t_{MM}=1.0$, $\Delta\varepsilon=1.0$, $\alpha=0.6$, $\beta=1.8$, $U_M=3.0$, $U_X=1.0$, $V_{MM}=0.5$, and $V_{MX}=1.0$ (M-CDW); $t_{MM}=1.0$, $\Delta\varepsilon=1.0$, $\alpha=1.8$, $\beta=0.6$, $U_M=3.0$, $U_X=1.0$, $V_{MM}=0.5$, and $V_{MX}=1.0$ (X-CDW); $t_{MM}=1.0$, $\Delta\varepsilon=0.2$, $\alpha=0.6$, $\beta=1.8$, $U_M=4.0$, $U_X=3.0$, $V_{MM}=1.0$, and $V_{MX}=0.5$ (M-SDW); and $t_{MM}=1.0$, $\Delta\varepsilon=0.2$, $\alpha=0.6$, $\beta=1.8$, $U_M=4.0$, $U_X=3.0$, $V_{MM}=0.5$, and $V_{MX}=1.0$ (X-SDW), where the M-CDW-, X-CDW-, M-SDW-, and X-SDW-type ground states are, respectively, obtained within the Hartree-Fock approximation. The four parametrizations are indicated by asterisks in Fig. 3.

B. Magnetic susceptibility

We show in Fig. 4 temperature dependences of the magnetic susceptibility χ peculiar to M-CDW, X-CDW, M-SDW, and X-SDW. At every temperature, we have taken several Monte Carlo estimates changing the Trotter number n_{T}, and their n_{T} dependence has been extrapolated to the $n_{\mathrm{T}}\rightarrow\infty$ limit. With decreasing temperature, the susceptibility shows a gentle upward slope and then exponentially vanishes in the CDW region, whereas in the SDW region it exhibits a significant enhancement, which is reminiscent of the low-temperature diverging behavior in Ni complexes.[15] The two CDW-proper susceptibilities show differences as well as similarities. The much more rapid low-temperature decrease in the X-CDW state is likely to denote spin-Peierls-like fluctuations. It is convincing that the susceptibility in the electronic-correlation-dominant region should also be saturated and turn and decrease at temperatures that are low enough to develop antiferromagnetic interactions between induced spin moments. However, the Monte Carlo estimates of the SDW-proper behavior at low temperatures are less convergent, where the numerical uncertainty is more than the symbol size. We should take special care how we understand the present SDW-proper susceptibilities, because no antiferromagnetic spin-density long-range order is stabilized purely in one dimension. If we calculate beyond the mean-field approximation, any SDW gap is not obtained but SDW-like fluctuations grow more and more with decreasing temperature in the relevant region. However, the slightest interchain coupling stabilizes such fluctuations into a long-range order. The SDW states[17,28] widely observed in Ni complexes are thus stabilized, where hydrogen bonds and/or van der Waals contacts supply weak but essential interchain interactions. Therefore, concerning the SDW states as well, the present calculations remain suggestive. We learn that induced local spin moments are larger in the M-SDW state than in the X-SDW state.

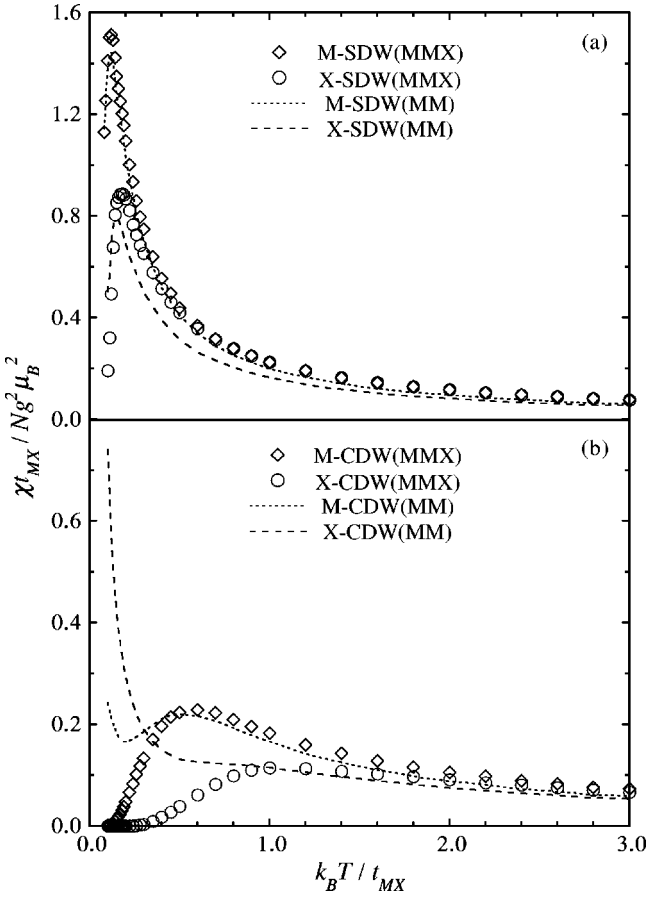

FIG. 5. Temperature dependences of the magnetic susceptibility (dotted and broken lines) on the assumption that the electrons occupying the X p_z orbitals make no contribution to the magnetization, together with those (open diamonds and circles) coming from all the electrons. Parametrizations are the same as those in Fig. 4.

In order to clarify the contribution from the X p_z orbitals, we carry out further calculations of the susceptibility separating magnetizations on the M_2 and X sublattices. We define the modified magnetic susceptibility $\chi^{(n_{\mathrm{orb}})}$ as

$$\chi^{(n_{\mathrm{orb}})}=\frac{g^2\mu_{\mathrm{B}}^2}{k_{\mathrm{B}}T}[\langle(M^{(n_{\mathrm{orb}})})^2\rangle_{\mathrm{th}}-\langle M^{(n_{\mathrm{orb}})}\rangle_{\mathrm{th}}^2], \qquad (3.3)$$

where $\langle\cdots\rangle_{\mathrm{th}}$ denotes the thermal average at a given temperature and

$$M^{(n_{\mathrm{orb}})}=\sum_{n=1}^{N}\sum_{i=1}^{n_{\mathrm{orb}}}\sum_{s=\pm}\frac{s}{2}n_{i:n,s}\,. \qquad (3.4)$$

The susceptibility coming from the M d_{z^2} orbitals, χ^{MM}, is given by $\chi^{(2)}$, while $\chi^{(3)}$ is the total susceptibility χ^{MMX}, which has just been shown in Fig. 4. We compare χ^{MM} with χ^{MMX} in Fig. 5. We find a clear contrast between χ^{MMX} and χ^{MM} in the parameter region stabilizing X-CDW to the

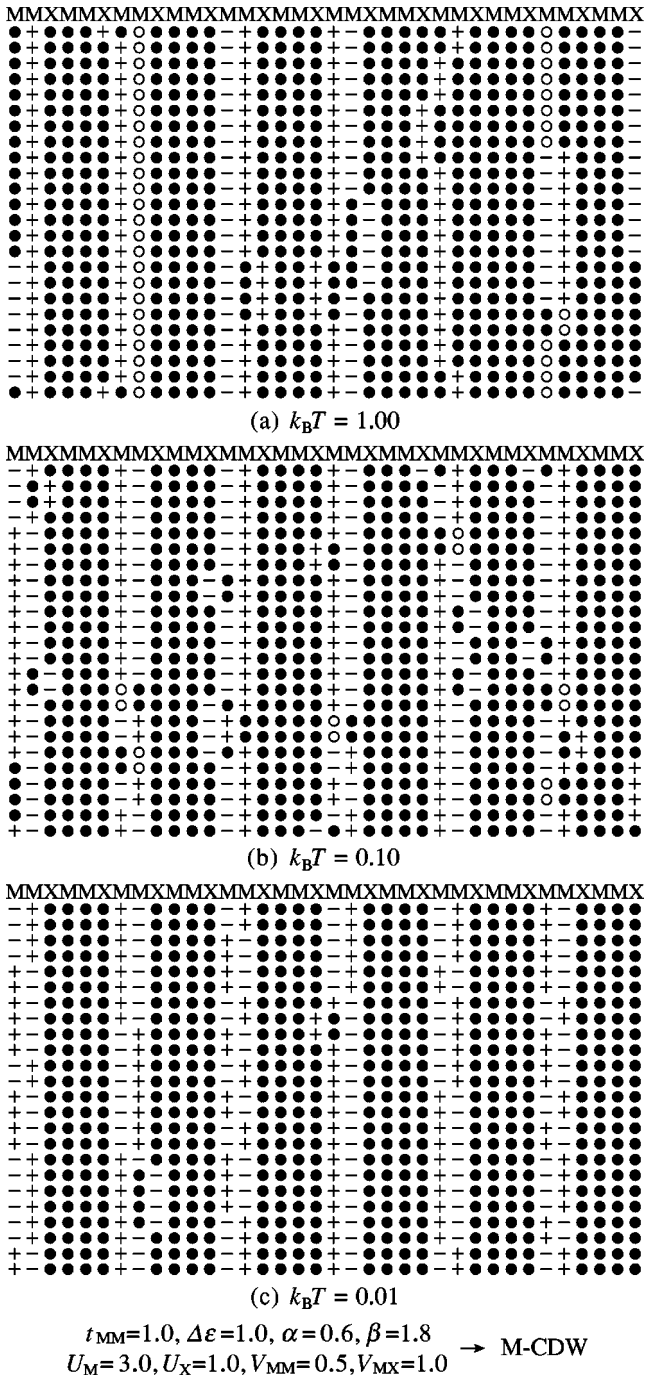

FIG. 6. Quantum Monte Carlo snapshots of the transformed two-dimensional Ising system of $N=12$, where the horizontal and the vertical axes correspond to space (the chain direction) and time (the Trotter direction), respectively. Trotter number n_T has been set equal to 12, 24, and 48, and the whole time passage $(1/k_BT)$, the former half of that $(1/2k_BT)$, and the first quarter of that $(1/4k_BT)$ are shown for $k_BT=1.00$, 0.10, and 0.01, respectively. + and − denote up and down spins, whereas ○ and ● represent vacant and doubly occupied sites, respectively. The parametrization is $t_{MM}=1.0$, $\Delta\varepsilon=1.0$, $\alpha=0.6$, $\beta=1.8$, $U_M=3.0$, $U_X=1.0$, $V_{MM}=0.5$, and $V_{MX}=1.0$, which stabilizes the *M*-CDW-type ground state.

ground state. Spin moments almost come from the M_2 sublattice at high temperatures, where the system is expected to lie in the averaged-valence state, while χ^{MM} more and more deviates from χ^{MMX} and exhibits a diverging behavior with decreasing temperature. Thus, the *X*-CDW state is never stabilized without the *p electrons* compensating the spin moments on the M_2 sublattice. The *M*-CDW state also exhibits such an aspect but it is much less remarkable. There exists a similar contrast between *M*-SDW and *X*-SDW as well. The halogen ions contribute no effective electron to the susceptibility in the *M*-SDW state, whereas all the electrons are effective in the *X*-SDW state. We stress again that the contribution from the *X* sublattice, $\chi^{MMX}-\chi^{MM}$, is not small in the *X*-SDW state, noting the different scales in Figs. 5(a) and 5(b).

C. Direct observation of the electronic states

Any path-integral method has the advantage of directly visualizing electronic states. We show in Figs. 6–9 Monte Carlo snapshots taken under the same parametrizations as the susceptibility calculations. Figures 6 and 7 clearly reveal the roles played by the *d* and *p* orbitals in the CDW states. The characteristic charge orders grow with decreasing temperature. In the ground state of the *M*-CDW type, the *X* p_z orbitals are almost completely filled, whereas oxidized halogen ions appear in every other unit in the *X*-CDW-type ground state. It is obvious that the alternate charge densities on the *X* sublattice, rather than the alternation of polarized charge densities on the M_2 sublattice, characterize the *X*-CDW state. Figures 8 and 9 also give a useful piece of information about the SDW states. The symmetry argument is concluded as follows: The antiferromagnetic spin ordering on the *X* sublattice characterizes *X*-SDW, where the *M* d_{z^2} orbitals also contribute spin moments favoring a parallel alignment within each *MXM* unit [Fig. 2(g)]; The antiferromagnetic spin ordering on the M_2 sublattice characterizes *M*-SDW, where the spin moments favor a parallel alignment within each M_2 moiety [Fig. 2(h)]. Figures 8 and 9 convincingly display all these properties. We stress in particular that the *X* p_z orbitals are all filled in Fig. 8(c), as well as in Fig. 6(c), which shows the single-band character of the *M*-type density-wave states well. Here we should be reminded that the present observations come from purely one-dimensional finite-chain calculations where any true antiferromagnetic *long-range* order can neither be stabilized nor be verified. The spin configuration indeed deviates from the perfect order peculiar to *X*-SDW here and there in Fig. 9(c). We find that domain walls prevent the characteristic local spin alignments from growing into the long-range order. Figure 8(c) just happens to contain no domain wall but longer-chain calculations still show the breakdown of the long-range order. It is, however, likely that *M*-SDW possesses more pronounced low-dimensional character than *X*-SDW.

It is also helpful in characterizing the SDW states to observe spin-spin correlations. We show in Fig. 10 spin correlation functions of a few types, which are defined as[42]

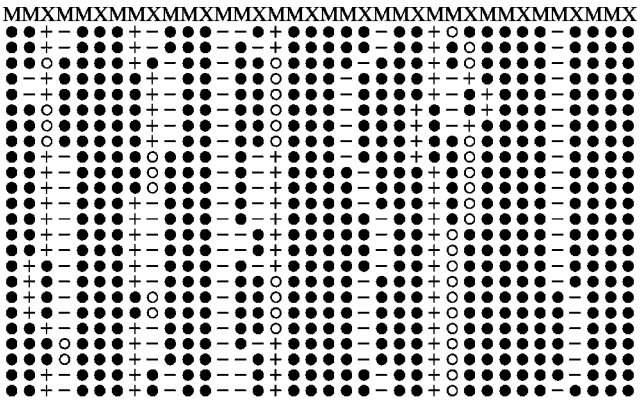

(a) $k_BT = 1.00$

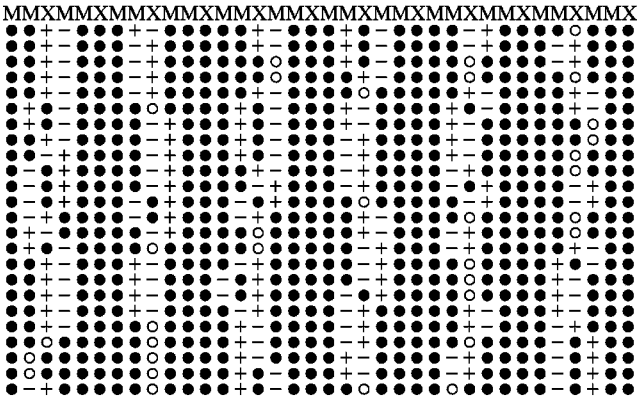

(b) $k_BT = 0.10$

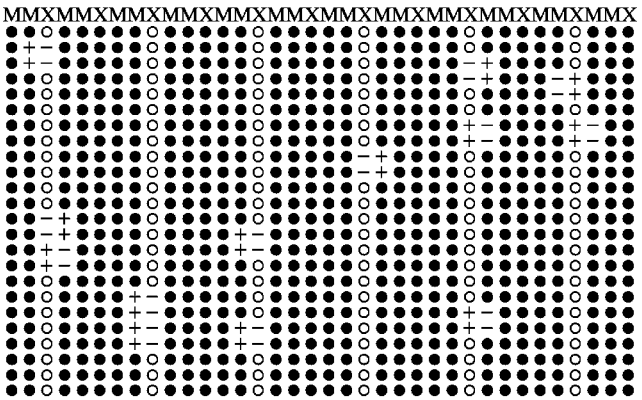

(c) $k_BT = 0.01$

$t_{MM}=1.0, \Delta\varepsilon=1.0, \alpha=1.8, \beta=0.6$
$U_M=3.0, U_X=1.0, V_{MM}=0.5, V_{MX}=1.0$ → X-CDW

FIG. 7. The same as Fig. 6 but $t_{MM}=1.0$, $\Delta\varepsilon=1.0$, $\alpha=1.8$, $\beta=0.6$, $U_M=3.0$, $U_X=1.0$, $V_{MM}=0.5$, and $V_{MX}=1.0$, which stabilizes the *X*-CDW-type ground state.

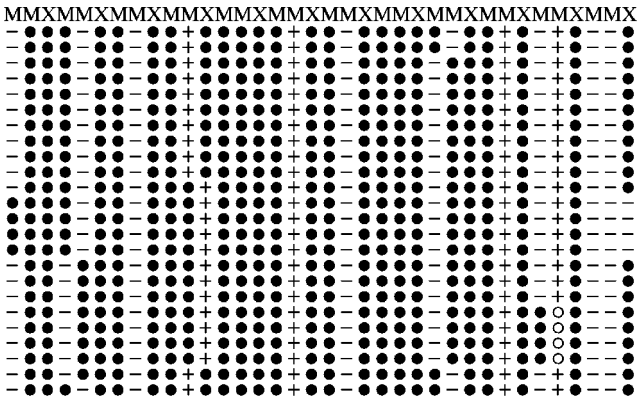

(a) $k_BT = 1.00$

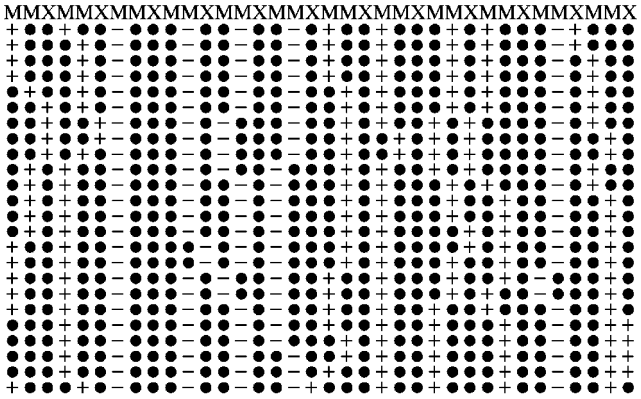

(b) $k_BT = 0.10$

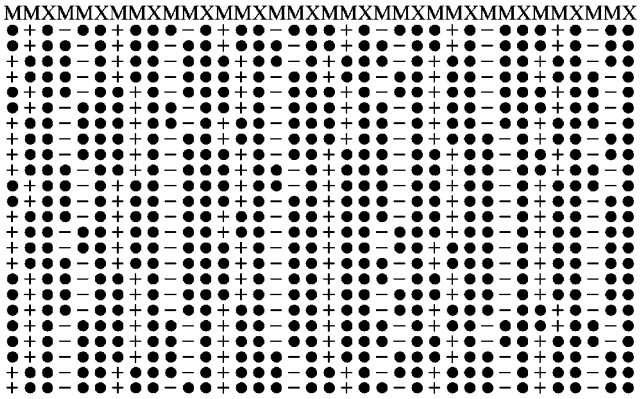

(c) $k_BT = 0.01$

$t_{MM}=1.0, \Delta\varepsilon=0.2, \alpha=0.6, \beta=1.8$
$U_M=4.0, U_X=3.0, V_{MM}=1.0, V_{MX}=0.5$ → M-SDW

FIG. 8. The same as Fig. 6 but $t_{MM}=1.0$, $\Delta\varepsilon=0.2$, $\alpha=0.6$, $\beta=1.8$, $U_M=4.0$, $U_X=3.0$, $V_{MM}=1.0$, and $V_{MX}=0.5$, which is expected to be favorable for the *M*-SDW-type ground state.

$$f^X(r)=\sum_{s,s'=\pm}\frac{ss'}{4}\langle n_{3:n,s}n_{3:n+r,s'}\rangle_{\mathrm{GS}},$$

$$f^{MM}(r)=\sum_{i,j=1}^{2}\sum_{s,s'=\pm}\frac{ss'}{4}\langle n_{i:n,s}n_{j:n+r,s'}\rangle_{\mathrm{GS}}, \quad (3.5)$$

$$f^{MXM}(r)=\sum_{i,j=1}^{3}\sum_{s,s'=\pm}\frac{ss'}{4}\langle n_{i:n,s}n_{j:n+r,s'}\rangle_{\mathrm{GS}},$$

where $\langle\cdots\rangle_{\mathrm{GS}}$ denotes the canonical average at absolute zero point and may approximately be identified with the Monte Carlo sampling without any global flip along the Trotter direction in the zero-magnetization subspace at a sufficiently low temperature.[43] In Fig. 10(a), no spin moment is essentially observed on the *X* sublattice, whereas there clearly exist antiferromagnetic spin-spin correlations on the M_2 sublattice. In Fig. 10(b), we find weak but surviving antiferromagnetic spin-spin correlations on the *X* sublattice. In the *X*-SDW state, the spin moments induced on the *X* sites

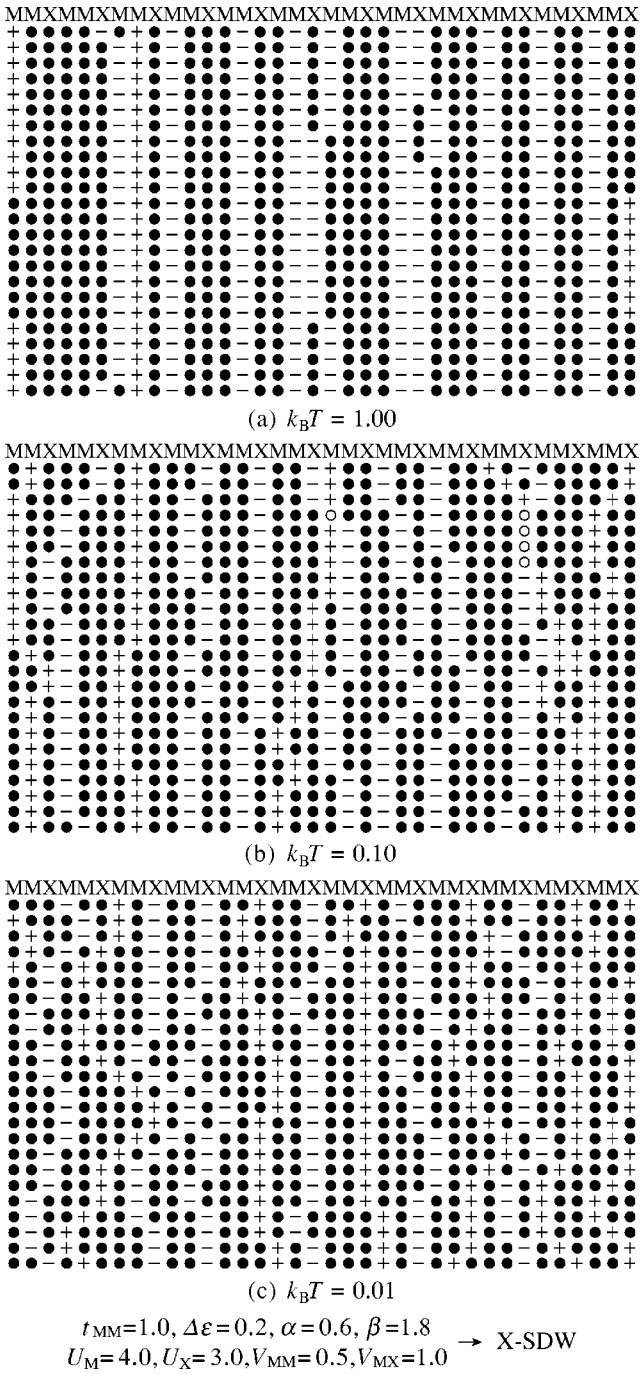

FIG. 9. The same as Fig. 6 but $t_{MM}=1.0$, $\Delta\varepsilon=0.2$, $\alpha=0.6$, $\beta=1.8$, $U_M=4.0$, $U_X=3.0$, $V_{MM}=0.5$, and $V_{MX}=1.0$, which is expected to be favorable for the *X*-SDW-type ground state.

are not as large as those on the M_2 moieties in the *M*-SDW state and their one-dimensional stabilization is less pronounced. However, observing $f^{MXM}(r)$ as well, we may fully be convinced of the symmetry properties illustrated in Fig. 2(g) and the two-band character of *X*-SDW.

Finally in this section, let us turn back to Figs. 6–9 and take a look at finite-temperature snapshots. The spin correlations do not survive thermal fluctuations at all within one dimension, while the charge correlations are rather tough

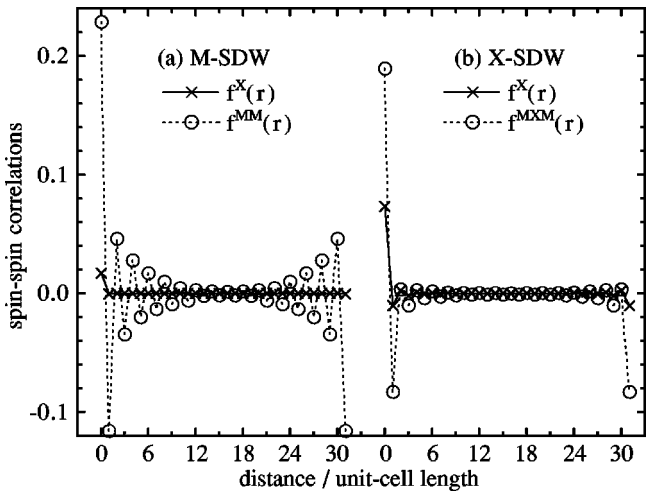

FIG. 10. Ground-state correlations between *r*-distant local spin moments on the *X* sites $[f^X(r)]$, the M_2 moieties $[f^{MM}(r)]$, and the MXM units $[f^{MXM}(r)]$ in the $N=32$ chain: (a) $f^X(r)$ and $f^{MM}(r)$ are shown by $\times$ and $\bigcirc$, respectively, under the same parametrization as Fig. 8; (b) $f^X(r)$ and $f^{MXM}(r)$ are shown by $\times$ and $\bigcirc$, respectively, under the same parametrization as Fig. 9. The solid and dotted lines are guides for eyes. It turns out that unless the Trotter number is large enough, the Monte Carlo estimates of ground-state spin-spin correlations for the present model are not so convergent but tend to be nonvanishingly frozen. Therefore, setting k_BT equal to 0.01, we thus present the conclusive calculations at a sufficiently large Trotter number, $n_T=200$, rather than extrapolate less convergent estimates at smaller Trotter numbers.

against increasing temperature. Such an aspect is more clearly demonstrated by *M*-CDW than by *X*-CDW. On the other hand, we have learned in Fig. 3 that *X*-CDW much more stably exists in the ground-state phase diagram. There may be a viewpoint that *M*-CDW is stable against thermal fluctuations but is sensitive to electronic correlations, while *X*-CDW is stable against quantum fluctuations but less survives thermal fluctuations. The *M*-CDW-type ground state is widely observed for the pop series of *MMX* chains,[21–25] whereas the *X*-CDW-type one is found for the dta complexes.[19,29] In $(NH_4)_4[Pt_2(pop)_4X]$, the valence structure of the *M*-CDW type remains stable, despite the minor formation of paramagnetic sites, up to room temperature.[24] On the other hand, $Pt_2(dta)_4I$ has been reported to undergo a phase transition from *X*-CDW to BOW around 80 K, far prior to the metallic behavior above 300 K.[29] These observations are qualitatively consistent with the present calculations. More extensive finite-temperature calculations will be reported elsewhere.

IV. SUMMARY AND DISCUSSION

We have investigated the electronic properties of *MMX* chains both analytically and numerically with particular emphasis on the *d*-*p*-hybridization effect on competing charge- or spin-ordered states. Density-wave states of the *M*-type,

M-CDW and *M*-SDW, may be described by a single-band model, whereas *p* electrons play an essential role in stabilizing those of the *X*-type, *X*-CDW and *X*-SDW. Such views of these density-wave states are further supported by their band dispersions shown in Fig. 11. In comparison with *M*-CDW, *X*-CDW exhibits much more widespread energy bands due to an essential hybridization between the *d* and *p* orbitals. Based on the present calculations together with the thus-far reported experimental observations, we characterize the pop and dta families of *MMX* compounds as d_{z^2}-single-band and *d*-*p*-hybridized two-band materials, respectively. Besides this viewpoint, *M*-CDW and *X*-CDW present a few contrasts between them: They are, respectively, stable and instable against thermal fluctuations while fragile and resistant in the ground-state phase diagram.

At the naivest consideration, single-band descriptions of *MMX* chains may more or less be justified unless $\Delta\varepsilon$ is small enough. However, this is not necessarily the case under the existence of electronic correlations. If we employ a single-band Hamiltonian[35]

$$\mathcal{H}=\frac{K}{2}\sum_{n}(l_{1:n}^{2}+l_{2:n}^{2})-\beta\sum_{n,s}(l_{1:n}n_{1:n,s}-l_{2:n}n_{2:n,s})$$

$$-\sum_{n,s}[t_{MXM}-\alpha(l_{1:n}-l_{2:n})](a_{1:n,s}^{\dagger}a_{2:n,s}+\text{H.c.})$$

$$-t_{MM}\sum_{n,s}(a_{1:n,s}^{\dagger}a_{2:n-1,s}+\text{H.c.})+U_{M}\sum_{n}(n_{1:n,+}n_{1:n,-}$$

$$+n_{2:n,+}n_{2:n,-})+\sum_{n,s,s'}V_{MM}n_{1:n,s}n_{2:n-1,s'}, \qquad (4.1)$$

the resultant phase diagrams are qualitatively consistent with the present calculations without any Coulomb interaction. Once we turn on U_X in the two-band Hamiltonian (2.1), the single-band model (4.1), no matter how well all the parameters are renormalized, considerably underestimates the stability of the M_2-sublattice-dimerized state in comparison with the present calculations. This fact is quite suggestive considering that U_X favors the oxidation of X^- ions. Though assignment of any parameter is not yet successfully done in *MMX* compounds, U_M and U_X must be larger than the transfer energy and be of the order of eV in analogy with

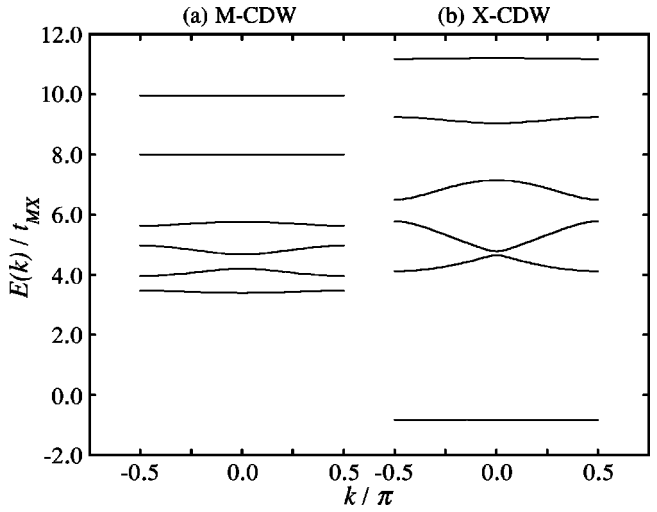

FIG. 11. Band dispersions peculiar to (a) *M*-CDW and (b) *X*-CDW, which are calculated within the Hartree-Fock approximation under the same parametrizations as Figs. 6 and 7, respectively.

MX compounds.[13] Thus an explicit treatment of the *X* p_z orbitals is indispensable to the dta complexes.

Experimental studies on halogen-bridged multinuclear metal complexes are still in the early stage. X-ray photoelectron spectroscopy measurements on $Pt_2(dta)_4I$ (Refs. 16 and 29) are now under controversy. Polymorphism inherent in the pop-family compounds, partly originating from the contained water molecules, sometimes prevent us from observing the proper behavior of these materials. We hope the present research will stimulate further measurements and lead to close collaboration between theoretical and experimental investigations.

ACKNOWLEDGMENTS

The author is grateful to K. Yonemitsu and M. Kuwabara for useful discussions. He is thankful to H. Okamoto, H. Kitagawa, and K. Kanoda as well for helpful comments on *MMX* materials and measurements on them. This work was supported by the Japanese Ministry of Education, Science, and Culture and by the Sanyo-Broadcasting Foundation for Science and Culture. The numerical calculation was done using the facility of the Supercomputer Center, Institute for Solid State Physics, University of Tokyo.

APPENDIX A: IRREDUCIBLE HAMILTONIANS

The irreducible Hamiltonians are

$$h_{\Gamma A}^{\lambda}=a_{\Gamma A}^{\lambda}\sum_{k,s,s'}(a_{1:k,s}^{\dagger}a_{1:k,s'}+a_{2:k,s}^{\dagger}a_{2:k,s'})\sigma_{ss'}^{\lambda}+b_{\Gamma A}^{\lambda}\sum_{k,s,s'}a_{3:k,s}^{\dagger}a_{3:k,s'}\sigma_{ss'}^{\lambda}+c_{\Gamma A}^{\lambda}\sum_{k,s,s'}[e^{-ik/3}a_{1:k,s}^{\dagger}a_{2:k,s'}\sigma_{ss'}^{\lambda}+\text{H.c.}]$$

$$+d_{\Gamma A}^{\lambda}\sum_{k,s,s'}[(e^{ik/3}a_{1:k,s}^{\dagger}a_{3:k,s'}+e^{-ik/3}a_{2:k,s}^{\dagger}a_{3:k,s'})\sigma_{ss'}^{\lambda}+\text{H.c.}], \qquad (A1)$$

$$h_{\Gamma B}^{\lambda}=a_{\Gamma B}^{\lambda}\sum_{k,s,s'}(a_{1:k,s}^{\dagger}a_{1:k,s'}-a_{2:k,s}^{\dagger}a_{2:k,s'})\sigma_{ss'}^{\lambda}+b_{\Gamma B}^{\lambda}\sum_{k,s,s'}[(e^{ik/3}a_{1:k,s}^{\dagger}a_{3:k,s'}-e^{-ik/3}a_{2:k,s}^{\dagger}a_{3:k,s'})\sigma_{ss'}^{\lambda}+\text{H.c.}], \qquad (A2)$$

$$h^{\lambda}_{XA}=a^{\lambda}_{XA}\sum_{k,s,s'}(e^{i\pi/3}a^{\dagger}_{1:k+\pi,s}a_{1:k,s'}+e^{-i\pi/3}a^{\dagger}_{2:k+\pi,s}a_{2:k,s'})\sigma^{\lambda}_{ss'}+b^{\lambda}_{XA}\sum_{k,s,s'}a^{\dagger}_{3:k+\pi,s}a_{3:k,s'}\sigma^{\lambda}_{ss'}$$

$$+c^{\lambda}_{XA}\sum_{k,s,s'}[(e^{i(k+\pi)/3}a^{\dagger}_{1:k+\pi,s}a_{3:k,s'}+e^{-i(k+\pi)/3}a^{\dagger}_{2:k+\pi,s}a_{3:k,s'})\sigma^{\lambda}_{ss'}+\mathrm{H.c.}], \tag{A3}$$

$$h^{\lambda}_{XB}=a^{\lambda}_{XB}\sum_{k,s,s'}(e^{i\pi/3}a^{\dagger}_{1:k+\pi,s}a_{1:k,s'}-e^{-i\pi/3}a^{\dagger}_{2:k+\pi,s}a_{2:k,s'})\sigma^{\lambda}_{ss'}+b^{\lambda}_{XB}\sum_{k,s,s'}[e^{-i(k-\pi)/3}a^{\dagger}_{1:k+\pi,s}a_{2:k,s'}\sigma^{\lambda}_{ss'}+\mathrm{H.c.}]$$

$$+c^{\lambda}_{XB}\sum_{k,s,s'}[(e^{i(k+\pi)/3}a^{\dagger}_{1:k+\pi,s}a_{3:k,s'}-e^{-i(k+\pi)/3}a^{\dagger}_{2:k+\pi,s}a_{3:k,s'})\sigma^{\lambda}_{ss'}+\mathrm{H.c.}], \tag{A4}$$

where

$$a^{0}_{\Gamma A}=\varepsilon_M-\frac{U_M}{2}+\left(\frac{U_M}{2N}+\frac{2V_{MM}}{N}\right)\sum_k[\rho^0_{11}(\Gamma;k)+\rho^0_{22}(\Gamma;k)]+\frac{4V_{MX}}{N}\sum_k\rho^0_{33}(\Gamma;k),$$

$$b^{0}_{\Gamma A}=\varepsilon_X-\frac{U_X}{2}+\frac{4V_{MX}}{N}\sum_k[\rho^0_{11}(\Gamma;k)+\rho^0_{22}(\Gamma;k)]+\frac{U_X}{N}\sum_k\rho^0_{33}(\Gamma;k),$$

$$c^{0}_{\Gamma A}=-t_{MM}-\frac{2V_{MM}}{N}\sum_k e^{ik/3}\rho^0_{12}(\Gamma;k),$$

$$d^{0}_{\Gamma A}=-t_{MX}-\frac{V_{MX}}{N}\sum_k[e^{-ik/3}\rho^0_{13}(\Gamma;k)+e^{ik/3}\rho^0_{23}(\Gamma;k)], \tag{A5}$$

$$a^{0}_{\Gamma B}=\left(\frac{U_M}{2N}-\frac{2V_{MM}}{N}-\frac{\beta^2}{KN}\right)\sum_k[\rho^0_{11}(\Gamma;k)-\rho^0_{22}(\Gamma;k)]+\frac{2\alpha\beta}{KN}\sum_k[e^{-ik/3}\rho^0_{13}(\Gamma;k)-e^{ik/3}\rho^0_{23}(\Gamma;k)],$$

$$b^{0}_{\Gamma B}=-\left(\frac{V_{MX}}{N}-\frac{2\alpha^2}{KN}\right)\sum_k[e^{-ik/3}\rho^0_{13}(\Gamma;k)-e^{ik/3}\rho^0_{23}(\Gamma;k)]+\frac{\alpha\beta}{KN}\sum_k[\rho^0_{11}(\Gamma;k)-\rho^0_{22}(\Gamma;k)], \tag{A6}$$

$$a^{0}_{XA}=\left(\frac{U_M}{2N}+\frac{2V_{MM}}{N}-\frac{\beta^2}{KN}\right)\sum_k[e^{i\pi/3}\rho^0_{11}(X;k)+e^{-i\pi/3}\rho^0_{22}(X;k)]+\frac{4V_{MX}}{N}\sum_k\rho^0_{33}(X,k)$$

$$+\frac{2\alpha\beta}{KN}\sum_k[e^{-ik/3}\rho^0_{13}(X;k)+e^{ik/3}\rho^0_{23}(X;k)],$$

$$b^{0}_{XA}=\frac{4V_{MX}}{N}\sum_k[e^{i\pi/3}\rho^0_{11}(X;k)+e^{-i\pi/3}\rho^0_{22}(X;k)]+\frac{U_X}{N}\sum_k\rho^0_{33}(X;k),$$

$$c^{0}_{XA}=-\left(\frac{V_{MX}}{N}+\frac{2\alpha^2}{KN}\right)\sum_k[e^{-ik/3}\rho^0_{13}(X;k)+e^{ik/3}\rho^0_{23}(X;k)]+\frac{\alpha\beta}{KN}\sum_k[e^{i\pi/3}\rho^0_{11}(X;k)+e^{-i\pi/3}\rho^0_{22}(X;k)], \tag{A7}$$

$$a^{0}_{XB}=\left(\frac{U_M}{2N}-\frac{2V_{MM}}{N}-\frac{\beta^2}{KN}\right)\sum_k[e^{i\pi/3}\rho^0_{11}(X;k)-e^{-i\pi/3}\rho^0_{22}(X;k)]+\frac{2\alpha\beta}{KN}\sum_k[e^{-ik/3}\rho^0_{13}(X;k)-e^{ik/3}\rho^0_{23}(X;k)],$$

$$b^{0}_{XB}=\frac{2V_{MM}}{N}\sum_k e^{i(k-\pi)/3}\rho^0_{12}(X;B),$$

$$c^{0}_{XB}=-\left(\frac{V_{MX}}{N}+\frac{2\alpha^2}{KN}\right)\sum_k[e^{-ik/3}\rho^0_{13}(X;k)-e^{ik/3}\rho^0_{23}(X;k)]+\frac{\alpha\beta}{KN}\sum_k[e^{i\pi/3}\rho^0_{11}(X;k)-e^{-i\pi/3}\rho^0_{22}(X;k)], \tag{A8}$$

$$a^{z}_{\Gamma A}=-\frac{U_M}{2N}\sum_k[\rho^z_{11}(\Gamma;k)+\rho^z_{22}(\Gamma;k)],$$

$$b^z_{\Gamma A}=-\frac{U_X}{N}\sum_k \rho^z_{33}(\Gamma;k),$$

$$c^z_{\Gamma A}=-\frac{2V_{MM}}{N}\sum_k e^{ik/3}\rho^z_{12}(\Gamma;k),$$

$$d^z_{\Gamma A}=-\frac{V_{MX}}{N}\sum_k [e^{-ik/3}\rho^z_{13}(\Gamma;k)+e^{ik/3}\rho^z_{23}(\Gamma;k)], \tag{A9}$$

$$a^z_{\Gamma B}=-\frac{U_M}{2N}\sum_k [\rho^z_{11}(\Gamma;k)-\rho^z_{22}(\Gamma;k)],$$

$$b^z_{\Gamma B}=-\frac{V_{MX}}{N}\sum_k [e^{-ik/3}\rho^z_{13}(\Gamma;k)-e^{ik/3}\rho^z_{23}(\Gamma;k)], \tag{A10}$$

$$a^z_{XA}=-\frac{U_M}{2N}\sum_k [e^{i\pi/3}\rho^z_{11}(X;k)+e^{-i\pi/3}\rho^z_{22}(X;k)],$$

$$b^z_{XA}=-\frac{U_X}{N}\sum_k \rho^z_{33}(X;k),$$

$$c^z_{XA}=-\frac{V_{MX}}{N}\sum_k [e^{-ik/3}\rho^z_{13}(X;k)+e^{ik/3}\rho^z_{23}(X;k)], \tag{A11}$$

$$a^z_{XB}=-\frac{U_M}{2N}\sum_k [e^{i\pi/3}\rho^z_{11}(X;k)-e^{-i\pi/3}\rho^z_{22}(X;k)],$$

$$b^z_{XB}=\frac{V_{MM}}{N}\sum_k e^{i(k-\pi)/3}\rho^z_{12}(X;k),$$

$$c^z_{XB}=-\frac{V_{MX}}{N}\sum_k [e^{-ik/3}\rho^z_{13}(X;k)-e^{ik/3}\rho^z_{23}(X;k)]. \tag{A12}$$

In obtaining the spatial-symmetry-definite order parameters (A5)–(A12), the lattice distortion has been described in terms of the electron density matrices so as to minimize the Hartree-Fock energy

$$\begin{aligned}\langle\mathcal{H}\rangle_{\mathrm{HF}}=&2\sum_{i,j}\sum_k \langle i{:}k|t|j{:}k\rangle\rho^0_{ji}(\Gamma;k)+2\sum_{i,j}\sum_k \langle i{:}k+\pi|t|j{:}k\rangle\rho^0_{ji}(X;k)+\sum_{i,j,m,n}\sum_{k,k'}(2\langle i{:}k;m{:}k'|v|j{:}k;n{:}k'\rangle\\
&-\langle i{:}k;m{:}k'|v|n{:}k';j{:}k\rangle)\rho^0_{ji}(\Gamma;k)\rho^0_{nm}(\Gamma;k')+\sum_{i,j,m,n}\sum_{k,k'}(2\langle i{:}k+\pi;m{:}k'|v|j{:}k;n{:}k'+\pi\rangle\\
&-\langle i{:}k+\pi;m{:}k'|v|n{:}k'+\pi;j{:}k\rangle)e^{(2\pi/3)i\delta_{m1}}e^{-(2\pi/3)i\delta_{m2}}\rho^0_{ji}(\Gamma;k)\rho^0_{nm}(\Gamma;k'+\pi)\\
&-\sum_{i,j,m,n}\sum_{k,k'}\langle i{:}k;m{:}k'|v|n{:}k';j{:}k\rangle\rho^z_{ji}(\Gamma,k)\rho^z_{nm}(\Gamma,k')-\sum_{i,j,m,n}\sum_{k,k'}\langle i{:}k+\pi;m{:}k'|v|n{:}k'+\pi;j{:}k\rangle\\
&\times e^{(2\pi/3)i\delta_{m1}}e^{-(2\pi/3)i\delta_{m2}}\rho^z_{ji}(\Gamma,k)\rho^z_{nm}(\Gamma,k'+\pi)+\frac{K}{2}\sum_{q=0,\pi}[(u_{3:q}-e^{iq/3}u_{1:q})^2+(u_{3:q}-e^{-iq/3}u_{2:q})^2].\end{aligned} \tag{A13}$$

Considering that the density matrices should possess the same symmetry properties as the irreducible Hamiltonian to which they belong, the coefficients (A5)–(A12) all turn out to be real.

APPENDIX B: CHARACTERIZATION OF THE DENSITY-WAVE SOLUTIONS

The density-wave solutions are characterized as follows.

(a) $\Gamma A\otimes\check{S}^0\otimes\check{T}^0$:

$$d_{1:n}=d_{2:n}=\frac{2}{N}\sum_k \bar{\rho}^0_{11}(\Gamma;k),\quad d_{3:n}=\frac{2}{N}\sum_k \bar{\rho}^0_{33}(\Gamma;k),$$

$$p_{1:n;2:n-1}=\frac{2}{N}\sum_k\left[\bar{\rho}^0_{12}(\Gamma;k)\cos\frac{k}{3}-\tilde{\rho}^0_{12}(\Gamma;k)\sin\frac{k}{3}\right],$$

$$p_{1:n;3:n}=p_{2:n;3:n}=\frac{2}{N}\sum_k\left[\bar{\rho}^0_{13}(\Gamma;k)\cos\frac{k}{3}+\tilde{\rho}^0_{13}(\Gamma;k)\sin\frac{k}{3}\right].$$

(b) $\Gamma B\otimes\check{S}^0\otimes\check{T}^0$

$$d_{i:n}=\frac{2}{N}\sum_k \bar{\rho}^0_{ii}(\Gamma;k)\quad (i=1,2,3),$$

$$p_{1:n;2:n-1}=\frac{2}{N}\sum_k\left[\bar{\rho}^0_{12}(\Gamma;k)\cos\frac{k}{3}-\tilde{\rho}^0_{12}(\Gamma;k)\sin\frac{k}{3}\right],$$

$$p_{1:n;3:n}=\frac{2}{N}\sum_k\left[\bar{\rho}^0_{13}(\Gamma;k)\cos\frac{k}{3}+\tilde{\rho}^0_{13}(\Gamma;k)\sin\frac{k}{3}\right],$$

$$p_{2:n;3:n}=\frac{2}{N}\sum_k\left[\bar{\rho}^0_{23}(\Gamma;k)\cos\frac{k}{3}-\tilde{\rho}^0_{23}(\Gamma;k)\sin\frac{k}{3}\right],$$

$$u_{3:n}=\frac{\beta}{KN}\sum_k\left[\bar{\rho}^0_{11}(\Gamma;k)-\bar{\rho}^0_{22}(\Gamma;k)\right]-\frac{2\alpha}{KN}\sum_k\left[\bar{\rho}^0_{13}(\Gamma;k)\cos\frac{k}{3}+\tilde{\rho}^0_{13}(\Gamma;k)\sin\frac{k}{3}-\bar{\rho}^0_{23}(\Gamma;k)\cos\frac{k}{3}+\tilde{\rho}^0_{23}(\Gamma;k)\sin\frac{k}{3}\right].$$

(c) $XA\otimes\check{S}^0\otimes\check{T}^0$:

$$d_{1:n}=d_{2:n}=\frac{2}{N}\sum_k \bar{\rho}^0_{11}(\Gamma;k)+\frac{2(-1)^n}{N}\sum_k\left[\bar{\rho}^0_{11}(X;k)\cos\frac{\pi}{3}-\tilde{\rho}^0_{11}(X;k)\sin\frac{\pi}{3}\right],$$

$$d_{3:n}=\frac{2}{N}\sum_k \bar{\rho}^0_{33}(\Gamma;k)+\frac{2(-1)^n}{N}\sum_k \bar{\rho}^0_{33}(X;k),$$

$$p_{1:n;2:n-1}=\frac{2}{N}\sum_k\left[\bar{\rho}^0_{12}(\Gamma;k)\cos\frac{k}{3}-\tilde{\rho}^0_{12}(\Gamma;k)\sin\frac{k}{3}\right],$$

$$p_{1:n;3:n}=p_{2:n;3:n}=\frac{2}{N}\sum_k\left[\bar{\rho}^0_{13}(\Gamma;k)\cos\frac{k}{3}+\tilde{\rho}^0_{13}(\Gamma;k)\sin\frac{k}{3}\right]+\frac{2(-1)^n}{N}\sum_k\left[\bar{\rho}^0_{13}(X;k)\cos\frac{k}{3}+\tilde{\rho}^0_{13}(X;k)\sin\frac{k}{3}\right],$$

$$u_{1:n}=-u_{2:n}=(-1)^n\left\{\frac{4\alpha}{KN}\sum_k\left[\bar{\rho}^0_{13}(X;k)\cos\frac{k}{3}+\tilde{\rho}^0_{13}(X;k)\sin\frac{k}{3}\right]-\frac{2\beta}{KN}\sum_k\left[\bar{\rho}^0_{13}(X;k)\cos\frac{\pi}{3}-\tilde{\rho}^0_{13}(X;k)\sin\frac{\pi}{3}\right]\right\}.$$

(d) $XB\otimes\check{S}^0\otimes\check{T}^0$:

$$d_{1:n}=\frac{2}{N}\sum_k \bar{\rho}^0_{11}(\Gamma;k)+\frac{2(-1)^n}{N}\sum_k\left[\bar{\rho}^0_{11}(X;k)\cos\frac{\pi}{3}-\tilde{\rho}^0_{11}(X;k)\sin\frac{\pi}{3}\right],$$

$$d_{2:n}=\frac{2}{N}\sum_k \bar{\rho}^0_{11}(\Gamma;k)-\frac{2(-1)^n}{N}\sum_k\left[\bar{\rho}^0_{11}(X;k)\cos\frac{\pi}{3}-\tilde{\rho}^0_{11}(X;k)\sin\frac{\pi}{3}\right],$$

$$d_{3:n}=\frac{2}{N}\sum_k \overline{\rho}^0_{33}(\Gamma;k),$$

$$p_{1:n;2:n-1}=\frac{2}{N}\sum_k\left[\overline{\rho}^0_{12}(\Gamma;k)\cos\frac{k}{3}-\tilde{\rho}^0_{12}(\Gamma;k)\sin\frac{k}{3}\right]-\frac{2(-1)^n}{N}\sum_k\left[\overline{\rho}^0_{12}(X;k)\cos\frac{k-\pi}{3}-\tilde{\rho}^0_{12}(X;k)\sin\frac{k-\pi}{3}\right],$$

$$p_{1:n;3:n}=\frac{2}{N}\sum_k\left[\overline{\rho}^0_{13}(\Gamma;k)\cos\frac{k}{3}+\tilde{\rho}^0_{13}(\Gamma;k)\sin\frac{k}{3}\right]+\frac{2(-1)^n}{N}\sum_k\left[\overline{\rho}^0_{13}(X;k)\cos\frac{k}{3}+\tilde{\rho}^0_{13}(X;k)\sin\frac{k}{3}\right],$$

$$p_{2:n;3:n}=\frac{2}{N}\sum_k\left[\overline{\rho}^0_{13}(\Gamma;k)\cos\frac{k}{3}+\tilde{\rho}^0_{13}(\Gamma;k)\sin\frac{k}{3}\right]-\frac{2(-1)^n}{N}\sum_k\left[\overline{\rho}^0_{13}(X;k)\cos\frac{k}{3}+\tilde{\rho}^0_{13}(X;k)\sin\frac{k}{3}\right],$$

$$u_{3:n}=(-1)^n\left\{\frac{4\alpha}{KN}\sum_k\left[\overline{\rho}^0_{13}(X;k)\cos\frac{k}{3}+\tilde{\rho}^0_{13}(X;k)\sin\frac{k}{3}\right]-\frac{2\beta}{KN}\sum_k\left[\overline{\rho}^0_{13}(X;k)\cos\frac{\pi}{3}-\tilde{\rho}^0_{13}(X;k)\sin\frac{\pi}{3}\right]\right\}.$$

(e) $\Gamma A\otimes\check{S}^1\otimes\check{T}^1$:

$$s^z_{1:n}=s^z_{2:n}=\frac{1}{N}\sum_k\overline{\rho}^z_{11}(\Gamma;k),\quad s^z_{3:n}=\frac{1}{N}\sum_k\overline{\rho}^z_{33}(\Gamma;k),$$

$$t^z_{1:n;2:n-1}=\frac{1}{N}\sum_k\left[\overline{\rho}^z_{12}(\Gamma;k)\cos\frac{k}{3}-\tilde{\rho}^z_{12}(\Gamma;k)\sin\frac{k}{3}\right],$$

$$t^z_{1:n;3:n}=t^z_{2:n;3:n}=\frac{1}{N}\sum_k\left[\overline{\rho}^z_{13}(\Gamma;k)\cos\frac{k}{3}+\tilde{\rho}^z_{13}(\Gamma;k)\sin\frac{k}{3}\right].$$

(f) $\Gamma B\otimes\check{S}^1\otimes\check{T}^1$:

$$s^z_{1:n}=-s^z_{2:n}=\frac{1}{N}\sum_k\overline{\rho}^z_{11}(\Gamma;k),\quad s^z_{3:n}=0,$$

$$t^z_{1:n;2:n-1}=0,\quad t^z_{1:n;3:n}=-t^z_{2:n;3:n}=\frac{1}{N}\sum_k\left[\overline{\rho}^z_{13}(\Gamma;k)\cos\frac{k}{3}+\tilde{\rho}^z_{13}(\Gamma;k)\sin\frac{k}{3}\right].$$

(g) $XA\otimes\check{S}^1\otimes\check{T}^1$:

$$s^z_{1:n}=s^z_{2:n}=\frac{(-1)^n}{N}\sum_k\left[\overline{\rho}^z_{11}(X;k)\cos\frac{\pi}{3}-\tilde{\rho}^z_{11}(X;k)\sin\frac{\pi}{3}\right],\quad s^z_{3:n}=\frac{(-1)^n}{N}\sum_k\overline{\rho}^z_{33}(X;k),$$

$$t^z_{1:n;2:n-1}=0,\quad t^z_{1:n;3:n}=t^z_{2:n;3:n}=\frac{(-1)^n}{N}\sum_k\left[\overline{\rho}^z_{13}(X;k)\cos\frac{k}{3}+\tilde{\rho}^z_{13}(X;k)\sin\frac{k}{3}\right].$$

(h) $XB\otimes\check{S}^1\otimes\check{T}^1$:

$$s^z_{3:n}=0,\quad s^z_{1:n}=-s^z_{2:n}=\frac{(-1)^n}{N}\sum_k\left[\overline{\rho}^z_{11}(X;k)\cos\frac{\pi}{3}-\tilde{\rho}^z_{11}(X;k)\sin\frac{\pi}{3}\right],$$

$$t^z_{1:n;2:n-1}=-\frac{(-1)^n}{N}\sum_k\left[\overline{\rho}^z_{12}(X;k)\cos\frac{k-\pi}{3}-\tilde{\rho}^z_{12}(X;k)\sin\frac{k-\pi}{3}\right],$$

$$t^z_{1:n;3:n}=-t^z_{2:n;3:n}=\frac{(-1)^n}{N}\sum_k\left[\overline{\rho}^z_{13}(X;k)\cos\frac{k}{3}+\tilde{\rho}^z_{13}(X;k)\sin\frac{k}{3}\right].$$

[1] M.B. Robin and P. Day, in *Advances in Inorganic Chemistry and Radiochemistry*, edited by H.J. Emeleus (Academic, New York, 1967), Vol. 10, p. 217.
[2] P. Day, in *Low Dimensional Cooperative Phenomena*, edited by H.J. Keller (Plenum, New York, 1974), p. 191.
[3] H.J. Keller, in *Extended Linear Chain Compounds*, edited by J. S. Miller (Plenum, New York, 1982), p. 357.
[4] R.J.H. Clark, in *Advances in Infrared and Raman Spectroscopy*, edited by R.J.H. Clark and R.E. Hester (Wiley, New York, 1984) Vol. II, p. 95.
[5] H. Toftlund and O. Simonsen, Inorg. Chem. **23**, 4261 (1984).
[6] K. Toriumi, Y. Wada, T. Mitani, S. Bandow, M. Yamashita, and Y. Fujii, J. Am. Chem. Soc. **111**, 2341 (1989).
[7] H. Okamoto, T. Mitani, K. Toriumi, and M. Yamashita, Mater. Sci. Eng., B **13**, L9 (1992).
[8] B.I. Swanson, M.A. Stroud, S.D. Conradson, and M.H. Zietlow, Solid State Commun. **65**, 1405 (1988); M.A. Stroud, H.G. Drickamer, M.H. Zietlow, H.B. Gray, and B.I. Swanson, J. Am. Chem. Soc. **111**, 66 (1989).
[9] K. Nasu, J. Phys. Soc. Jpn. **52**, 3865 (1983); **53**, 302 (1984); **53**, 427 (1984).
[10] A.R. Bishop, J.T. Gammel, S.R. Phillpot, Synth. Met. **29**, F151 (1989); I. Batistić, J.T. Gammel, and A.R. Bishop, Phys. Rev. B **44**, 13 228 (1991).
[11] H. Röder, A.R. Bishop, and J.T. Gammel, Phys. Rev. Lett. **70**, 3498 (1993); J.T. Gammel, K. Yonemitsu, A. Saxena, A.R. Bishop, and H. Röder, Synth. Met. **55-57**, 3377 (1993).
[12] S. Yamamoto, Phys. Lett. A **247**, 422 (1998); Synth. Met. **103**, 2683 (1999).
[13] J.T. Gammel, A. Saxena, I. Batistić, A.R. Bishop, and S.R. Phillpot, Phys. Rev. B **45**, 6408 (1992); S.W. Weber-Milbrodt, J.T. Gammel, A.R. Bishop, and E.Y. Loh, Jr., *ibid.* **45**, 6435 (1992).
[14] H. Okamoto, Y. Kaga, Y. Shimada, Y. Oka, Y. Iwasa, T. Mitani, and M. Yamashita, Phys. Rev. Lett. **80**, 861 (1998).
[15] K. Marumoto, H. Tanaka, S. Kuroda, T. Manabe, and M. Yamashita, Phys. Rev. B **60**, 7699 (1999).
[16] C. Bellitto, A. Flamini, L. Gastaldi, and L. Scaramuzza, Inorg. Chem. **22**, 444 (1983).
[17] C. Bellitto, G. Dessy, and V. Fares, Inorg. Chem. **24**, 2815 (1985).
[18] C.-M. Che, F.H. Herbstein, W.P. Schaefer, R.E. Marsh, and H.B. Gray, J. Am. Chem. Soc. **105**, 4604 (1983).
[19] H. Kitagawa, N. Onodera, J.-S. Ahn, T. Mitani, K. Misa, Y. Ozawa, K. Toriumi, K. Yasui, T. Manabe, and M. Yamashita, Mol. Cryst. Liq. Cryst. Sci. Technol., Sect. A **285**, 311 (1996); H. Kitagawa, N. Onodera, J.-S. Ahn, T. Mitani, K. Toriumi, and M. Yamashita, Synth. Met. **86**, 1931 (1997).
[20] K. Sakai, Y. Tanaka, Y. Tsuchiya, K. Hirata, T. Tsubomura, S. Iijima, and A. Bhattacharjee, J. Am. Chem. Soc. **120**, 8366 (1998).
[21] M. Kurmoo and R.J.H. Clark, Inorg. Chem. **24**, 4420 (1985).
[22] R.J.H. Clark, M. Kurmoo, H.M. Dawes, and M.B. Hursthouse, Inorg. Chem. **25**, 409 (1986).
[23] L.G. Butler, M.H. Zietlow, C.-M. Che, W.P. Schaefer, S. Sridhar, P.J. Grunthaner, B.I. Swanson, R.J.H. Clark, and H.B. Gray, J. Am. Chem. Soc. **110**, 1155 (1988).
[24] N. Kimura, H. Ohki, R. Ikeda, and M. Yamashita, Chem. Phys. Lett. **220**, 40 (1994).
[25] Y. Wada, T. Furuta, M. Yamashita, and K. Toriumi, Synth. Met. **70**, 1195 (1995).
[26] S.D. Conradson, M.A. Stroud, M.H. Zietlow, B.I. Swanson, D. Baeriswyl, and A.R. Bishop, Solid State Commun. **65**, 723 (1988).
[27] M. Yamashita, S. Miya, T. Kawashima, T. Manabe, T. Sonoyama, H. Kitagawa, T. Mitani, H. Okamoto, and R. Ikeda, J. Am. Chem. Soc. **121**, 2321 (1999).
[28] H. Okamoto, Y. Shimada, Y. Oka, A. Chainani, T. Takahashi, H. Kitagawa, T. Mitani, K. Toriumi, K. Inoue, T. Manabe, and M. Yamashita, Phys. Rev. B **54**, 8438 (1996).
[29] H. Kitagawa, N. Onodera, T. Sonoyama, M. Yamamoto, T. Fukawa, T. Mitani, M. Seto, and Y. Maeda, J. Am. Chem. Soc. **121**, 10068 (1999).
[30] M. Ozaki, Prog. Theor. Phys. **67**, 83 (1982); **67**, 415 (1982).
[31] M. Ozaki, J. Math. Phys. **26**, 1514 (1985); **26**, 1521 (1985).
[32] M. Ozaki, Int. J. Quantum Chem. **42**, 55 (1992); S. Yamamoto and M. Ozaki, *ibid.* **44**, 949 (1992).
[33] S. Yamamoto and M. Ozaki, Solid State Commun. **83**, 329 (1992); **83**, 335 (1992).
[34] W.P. Su, J.R. Schrieffer, and A.J. Heeger, Phys. Rev. Lett. **42**, 1698 (1979); Phys. Rev. B **22**, 2099 (1980); **28**, 1138 (1983).
[35] M. Kuwabar and K. Yonemitsu, Mol. Cryst. Liq. Cryst. (to be published).
[36] S. Yamamoto, J. Phys. Soc. Jpn. **69**, 13 (2000).
[37] S.A. Borshch, K. Prassides, V. Robert, and A.O. Solonenko, J. Chem. Phys. **109**, 4562 (1998).
[38] D. Baeriswyl and A.R. Bishop, Phys. Scr. **T19**, 239 (1987); J. Phys. C **21**, 339 (1988).
[39] S. Yamamoto, Phys. Lett. A **258**, 183 (1999).
[40] M. Suzuki, Prog. Theor. Phys. **56**, 1454 (1976).
[41] J.E. Hirsch, D.J. Scalapino, R.L. Sugar, and R. Blankenbecler, Phys. Rev. Lett. **47**, 1628 (1981); J.E. Hirsch, R.L. Sugar, D.J. Scalapino, and R. Blankenbecler, Phys. Rev. B **26**, 5033 (1982).
[42] H. Onishi and S. Miyashita, J. Phys. Soc. Jpn. **69**, 2634 (2000).
[43] S. Yamamoto, Phys. Rev. B **52**, 10 170 (1995).